Chair of Ferrous Metallurgy

Master's Thesis

Ultra-Clean Steel Production: Behavior of Micro-Sized Alumina Inclusions at The Ar Gas/Liquid Steel Interface

Ahmed Ibraheem, BSc.

September 2022

AFFIDAVIT

I declare on oath that I wrote this thesis independently, did not use other than the specified sources and aids, and did not otherwise use any unauthorized aids.

I declare that I have read, understood, and complied with the guidelines of the senate of the Montanuniversität Leoben for "Good Scientific Practice".

Furthermore, I declare that the electronic and printed version of the submitted thesis are identical, both, formally and with regard to content.

Date 16.02.2023

Signature Author
Ahmed Mohamed Ibraheem

KU LEUVEN

FACULTEIT INGENIEURSWETENSCHAPPEN

Ultra-clean steel production: Micro-sized alumina inclusions behavior at the Ar gas/liquid steel interface

Ahmed Ibraheem

Academic year 2021 – 2022

Master of Science in Materials Engineering

Ultra-clean steel production: Micro-sized alumina inclusions behavior at the Ar gas/liquid steel interface

Ahmed Ibraheem

Academic year 2021 – 2022

Preface

This thesis was submitted as completion for my degree of Master in Materials Engineering, option Sustainable Materials, at KU Leuven. The project was proposed by my promotor Prof. Dr. Ir. Bart Blanpain and Dr. Ir. Muxing Guo. The experimental work was mainly performed at the Department of Materials Engineering (MTM, KU Leuven).

I would like to express my gratitude to Prof. Bart Blanpain and Dr. Ir. Muxing Guo for their support. It was my pleasure to be introduced to this domain. I learnt a lot about colloid and interface science, and non-metallic inclusions in steel. I would like to give extra thanks to my mentor Zilong Qiu for his daily collaboration, patience, and feedback. He helped and guided me throughout this thesis project with the experiments we performed in the lab and with writing the thesis. I learnt so much and it was a pleasure working with him. Finally, I would like to thank all the people at MTM and the other departments, for their technical assistance in the laboratories: Joris Vandyck, Iris Cuppens, and Christel Butnaru and all the other people I forgot.

Thank you very much to everybody who made this thesis possible. Also, a great thanks goes to my family, friends, and co-students for their support.

Ahmed Ibraheem

Table of Contents

Abstract

Nowadays, as the industry is shifting towards more sustainability, the demand for Ultra-clean steel (UCS) is rising. UCS is used in several critical engineering applications where superior specifications are required. At this high level of cleanliness, the presence of even a very small number of inclusions exceeding the critical size can have serious effects on the quality of steel. Numerous methods were developed to improve the cleanliness of steel by minimizing the content of impurities and mitigating the effects of the inevitably occurring content by transforming them into less harmful impurities. The most common cleaning method is to inject argon gas bubbles which pick up the inclusions from the liquid steel bath and transfer them to slag.

Non-metallic inclusions (NMIs) are inseparable from the steel making process. They originate from several sources, including deoxidation and reoxidation, refractory liner, the flux, the iron ore, and/or the scrap. NMIs are classified according to numerous criteria, including their origins, their sizes, their chemical composition, and their acidic and alkaline behavior. One of the most common inclusion types -especially in producing Al-killed steel- is alumina inclusions. This type of inclusion has harmful effects on the Continuous casting (CC) process as it leads to the arising of the phenomenon of clogging in the submerged entry nozzle (SEN). Additionally, alumina inclusions affect the steel's mechanical properties since it acts as a crack initiation site that decreases the toughness of steel.

Alumina inclusions though usually distributed homogeneously over the melt surface, form clusters rapidly. The phenomenon of clustering of NMIs at the surface of liquid steel is attributed to lateral capillary interaction, which depends on the deformation of the meniscus around. The uniform deformation of the 3-phase contact line between the solid inclusion particle, liquid steel, and the atmosphere (argon gas) occurs under the effect of the inclusion weight. In this case, the micro-sized inclusions are treated as "capillary charges". In the case of micro inclusions having negligible masses, the meniscus deformation due to particle weight is negligible. However, it was found that the floating particles still strongly attract each other. Another mechanism was proposed that the meniscus is not uniformly deformed but in an undulated manner. In this case, the capillary charge is replaced by the term 'capillary multipole' where the type of interaction depends on the meniscus undulation amplitude and the orientation of the floating particle. The attraction force between alumina inclusions floating at the interface between liquid steel and argon gas was investigated using the confocal laser scanning microscope (CSLM) which is capable of in-situ observation of the NMIs behavior at the liquid steel/argon gas interface. The interactions of alumina inclusions were interpreted using the capillary multipole model. The results of 13 cases were analyzed and compared, and the type of lateral capillary interaction was discussed. The dipole-quadrupole model was the best model to interpret the interaction force between alumina inclusions.

List of figures

List of tables

Lists of abbreviations and symbols

List of abbreviations
UCS   Ultra-clean steel
NMIs   Non-metallic inclusions
CC   Continuous casting
CSLM   Confocal scanning laser microscope
LF   Ladle furnace
VD   Vacuum degassing
EAF   Electric arc furnace
BOF   Basic oxygen furnace
SEN   Submerged entry nozzle
CAH   Contact angle hysteresis
RMDS Random middle deviation of squares
SEM   Scanning electron microscope
EDS   Energy dispersive spectroscopy
SSR   Sum of squared residuals
DP   Dipole
QP   Quadrupole
HP   Hexapole

List of symbols

σ Surface tension [N/m]

σ_{SG} Surface tension at solid gas interface [N/m]

σ_{SL} Surface tension at solid liquid interface [N/m]

σ_{GL} Surface tension at gas liquid interface [N/m]

ψ_k Slope angle of contact line of particle k

α Contact angle

$\Delta\alpha$ Contact angle hysteresis

α_v Advancing contact angle

α_R Receding contact angle

R_k Radius of particle k [m]

b_k Contact line radius of particle k [m]

H_k Contact line undulation amplitude [m]

W_g Gravitational energy [J]

W_w	Wetting energy [J]
W_m	Meniscus energy [J]
W	System free energy [J]
ΔW	Capillary interaction energy [J]
q^{-1}	Capillary length [m]
Q	Capillary charge [m]
K_1	Modified Bessel function of first order
L	Interparticle distance [m]
g	Gravitational acceleration [m/s^2]
h_k	Mean elevation of contact line of particle k [m]
φ_k	Angle of rotation of particle k
ρ_I	Density of liquid phase [kg/m^3]
ρ_{II}	Density of gaseous phase [kg/m^3]
F_{cap}	Capillary force [N]
F_{drag}	Drag force [N]
f	Drag coefficient
μ	Fluid viscosity [N.s/m^2]
v	Flow velocity [m/s]
m_k	Mass of particle k [kg]
Δt	Time interval [s]
G^{-1}	Mobility function
n_k	Multipole order of particle k
S_{res}	Sum of squared regression of the differences between drag and capillary forces
S_{tot}	Total sum of squares of differences between drag and capillary forces
R^2	Coefficient of determination
k	Boltzmann constant [J/K]

Chapter one: Introduction

The development of steel-making industry is an ongoing process, with the aim to make it more sustainable and to improve the quality of steel to meet the needs of modern industries. One of the most important goals of steel making is to limit the NMIs content in steel. The maximum allowable inclusion content varies among different grades of steel [1,2]. UCSs are needed in special engineering applications such as some transportation equipment. These steels are used in high stress conditions; therefore, even very small content of inclusions or impurities can be detrimental for their mechanical properties.

Several improvements have been introduced to steel making process to enhance the cleanliness of steel [3,4]. One of the main cleaning methods currently applied is using argon gas bubbles to pick up inclusions from the steel bath and move them to the surface. For this process to be more efficient the inclusions should agglomerate into larger clusters to be easier to pick them up. On the other hand, larger clusters of inclusions if left in steel can greatly deteriorate its quality. Therefore, the behavior of inclusions on the liquid steel/argon gas interface and their tendency to agglomerate and form clusters are investigated. Several studies were carried out on different inclusion materials. These studies confirmed that there is an attraction force between NMIs. The magnitude of this force varies from one material to another. This phenomenon was attributed to lateral capillary interaction between floating particles. Several theoretical models were introduced and modified to explain this phenomenon.

On top of NMIs in steel is alumina inclusions which can come from different sources. Aluminum is added to steel to control the grain size and to clean it from oxygen gas. When aluminum reacts with oxygen it can produce fine particles of alumina which remain in the steel bath. In addition, alumina can come from refractories. Therefore, alumina inclusions in steel cannot be completely avoided. Beside the same bad effects caused by other inclusions on the mechanical properties, alumina inclusions also contribute to nozzle clogging which badly affects the CC process. Therefore, it is important to understand the behavior of alumina and specially the micro-sized inclusions to mitigate their harmful effects on the CC process and the properties of steel [5]. Capillary interaction models were applied in previous studies on different types of inclusions, however, the identification of the type of interaction between alumina inclusions was not investigated before.

Lateral capillary interaction was first introduced by Nicolson [6] who attributed the capillary force to the gravitational force of the floating particles. A new model was then introduced by Paunov et al. [7] where they included the contributions of wettability and liquid meniscus. Yin et al. were the first to analyze the attraction force between alumina particles [8]. They explained this attraction force by the depression of the surrounding liquid surface around the approaching particles. This depression leads to a capillary pressure difference between the outside and the inside area of the particles which pushes the particles towards each other [9]. These theories however, failed to

justify the observed strong attraction force associated with small particles which have negligible weights. Afterwards, Stamou et al. [10] referred to the non-uniform meniscus shape and its contribution to capillary interaction. When the particle is chemically heterogeneous, has an irregular shape, or a rough surface, the liquid meniscus around it will be pinned at some positions to the surface of the particle, which will make the shape of the meniscus nonuniform (undulated) in the sense that the meniscus will be lower than the average at some positions and higher at other positions. Finally, Danov et al. [11] introduced a theoretical model to describe the capillary interaction between particles of non-uniform meniscus. This model showed that the deformation of the contact line with the liquid interface can lead to a great increase in the attraction force. And thus, it justified the large attraction force between very small particles.

The aim of this thesis is to understand the strong capillary attraction between micro-alumina inclusions at the Argon/liquid steel interface. it has been proposed that the capillary interaction between these particles depends on the deformation of the interface caused by the undulated contact line. In the case of alumina micro inclusions, the undulation type influencing the attraction force between the particles is still unknown. To determine it, the position of the particles approaching each other at the interface is recorded during the *in-situ* observation of the alumina particles at the interface of liquid steel and argon gas using confocal scanning microscopy (CLSM). Then based on these recorded image sequences, the velocity and acceleration of these particles are calculated with the help of MATLAB software. Using the theoretical models for undulated contact line shown before, the theoretical capillary force is estimated and compared to the experimental results. Experimental results are compared to different multipole models in an attempt to figure out the order of magnitude of undulation on each of the interacting particles. Understanding the nature of the force acting on them will help predict the behavior of these inclusions and, in particular, their clustering rate and thus, improve their removal methods and the steel cleanliness.

This thesis consists of four chapters beside the introduction: Chapter two consists of two parts. The first part presents the literature review on NMIs in steel, their origins, and some of the methods for treating them. In the second part, the theory of lateral capillary interaction with its modifications are explained. In chapter three, the experimental methods used to investigate the behavior of NMIs were introduced. In chapter four, the results obtained from the observation of NMIs floating on liquid steel surface were presented, analyzed, and discussed. Finally, in chapter five, the conclusions of this thesis are presented.

Chapter two: Literature review

This chapter is divided into two sections. In the first section, the characteristics of NMIs in steel are presented. The types of inclusions based on different classification criteria, and different origins of inclusions throughout the steel making process are introduced. In addition, the state of art in cleaning steel from NMIs is reviewed, particularly, the methods including Ar gas purging. In the second section, the theories proposed to explain the behavior of NMIs floating on the surface if liquid steel are presented. First an overview of the basic terms such as surface tension, meniscus, and contact angle are given. Then the theoretical and experimental work carried out to explain the behavior of floating particles are summarized.

2.1. Characterization of NMIs

Steel making is classified into two main process types, primary and secondary steel making. In primary steel making, iron ore is reduced in the Blast furnace to produce pig iron which has high carbon content. Pig iron is then introduced to the Basic oxygen furnace (BOF) in which oxygen is blown into the bath to lower the carbon content and produce steel. In the case of secondary steel making, steel scrap is melted in the electric arc furnace (EAF) and then mixed with carbon and flux to produce refined steel. In both types of steel making, Removing NMIs and impurities is an important process parameter which defines the quality of the produced steel. These NMIs include carbon, sulfur, phosphorous, and nitrogen. In addition, alloying elements are introduced (e.g., Mn, Al, Ni, B, Mo, Ti, Cr, V), which gives the steel improved mechanical and physical properties that allow it to be utilized in various structural and mechanical applications [12]. Nonetheless, it is almost impossible to completely eliminate NMIs or avoid their entrapment to steel.

NMIs are chemical compounds non-intentionally trapped in steel that originated from deoxidation, reoxidation and exogenous processes [3]. Typical examples are oxides, nitrides, and sulfides, but also oxysulfides, carbonitrides, and complex compounds such as $MgO.Al_2O_3$. Inclusions can be ionic, covalent, or mixed bonded. They are generally brittle at room temperature and are weakly bonded to the metallic matrix [13]. Therefore, NMIs are typically very harmful to steel, especially large and hard inclusions [13]. In addition, the shape of the NMI has a significant effect on the properties of steel. Sometimes NMIs have a sharp-edged interface with the steel matrix, which could be detrimental to the mechanical properties (e.g., toughness) and these sites act as crack initiation sites. Nevertheless, sometimes having NMIs in steel can be beneficial to its properties if these inclusions are well controlled. For example, MnS improves the machinability of steel [14,15]. In addition, NMIs can act as nucleation sites for heterogenous nucleation during solidification, which enhances grain refinement. For most applications, however, it is important to produce clean steel. For special application steels, high cleanliness and control of inclusions are necessary [16]. The general rule is that the fewer or less severe the inclusions, the higher the steel quality. Therefore, controlling, analyzing, and documenting NMIs are important for quality control [17].

NMIs are classified according to several criteria, including the source, the size, the chemical composition, and the time of formation. Regarding the source of inclusions, NMIs are generally divided into endogenous and exogenous. Endogenous inclusions are defined as inclusions which emerge from the steel making process such as oxides and sulfides. Endogenous inclusions include deoxidation products which are produced due to the reaction between dissolved oxygen and added deoxidant (e.g., Al in killed steel, Si in semi-killed steel). On the other hand, exogenous inclusions are defined as those originating from external sources such refractory fragments mixing with liquid steel and slag entrapments [18]. These entrapments form liquid inclusions that are usually spherical. Other sources could be loose dirt, and ceramic lining fragments generated by erosion. These inclusions are mostly large and have irregular shapes. However, most of the time, exogenous inclusions do not maintain their state in liquid steel for long. They readily react with the steel and change greatly [2,19]. Exogenous inclusions also include reoxidation products which are defined as inclusions produced when the remaining tramp elements in liquid steel react with FeO or when they are exposed to the atmosphere and form oxides like Al_2O_3 [20].

With respect to size, inclusions are divided into three main groups: (1) macro-inclusions, (2) meso-inclusions, and (3) micro-inclusions. In principle, macro-inclusions have large sizes such as they can cause an immediate failure of steel during manufacturing or application. Otherwise, inclusions are classified as meso or micro-inclusions. However, it is difficult to apply this principle in practice [2]. Generally, macro-inclusions are those which are larger than 100 μm [21]. They are mostly formed due to reoxidation of entrapments or deoxidation elements, ladle slag carryover, slag emulsification, or refractory erosion [22]. The maximum inclusion size determines the quality of steel, the smaller the allowed maximum inclusion size, the higher the quality of steel. Macro-inclusions are allowed only in the case of concrete steel and structural steel. Inclusions of sizes ranging from 30 to 100 μm are called meso-inclusions. Finally, Micro-inclusions are those who have a size ranging between 1 to 30 μm, and they are typically deoxidation products. Steel grades of relatively high-quality requirements allow only micro-inclusions. Those include bearing steel, line pipe steel, heavy plate steel, plastic mold steel and to a less extent: tire cord and aerospace alloys [17].

It was observed that NMIs floating at the surface of liquid steel attract each other, agglomerate, and form larger clusters [8]. If these clusters remain in steel, they will deteriorate steel's mechanical properties. Inclusion size has an evident role in both the strength and the hardness of steel as large macro-inclusions can greatly deteriorate the mechanical properties of steel [23]. For this reason, the maximum size of NMIs is restricted in many steel grades [24]. Figure 2.1 shows the effect of NMIs size on the strength of a steel alloy. Large inclusions are usually much fewer than micro-inclusions as the former can be relatively easier to be removed; however, they can have a larger total volume fraction compared to micro-inclusions. In certain cases, even one single macro inclusion can cause a catastrophic defect in a whole slab or billet [20]. Besides the size, the shape of the NMI has a significant effect on the properties of steel as well. Sometimes NMIs have sharp edges, which act as crack initiation sites and again this could be significantly reduce the mechanical properties such as toughness.
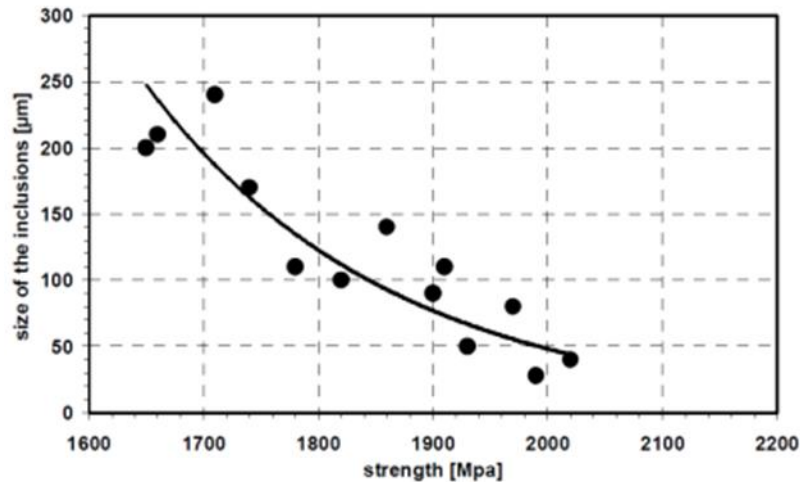
Figure 2.1. The relation between inclusion size and strength of 54SiCrV6 alloy [25].

Even at a very low volume fraction, NMIs play a vital role in the properties of steel. Some steel properties are significantly affected by NMIs, such as ductile fracture, corrosion resistance, fatigue strength, welding properties, machinability, and surface polishing. NMIs are responsible for the arising of several defects in steel. For example, they result in a drop of the formability of Al-killed steel, which induces cracks in Al-killed steel products such as flanges. Besides, NMIs in axels and bearings reduce the lifetime of these products and increase their susceptibility to fatigue [3,20]. Another property of NMIs that downgrades the mechanical properties of steel is that they usually have a weak bonding to the metallic matrix. Cracking or debonding of NMIs results in the generation of micro-voids within the steel microstructure. The growth and coalescence of those micro-voids lead to ductile fracture [26].

Even though NMIs mostly pose negative effects on steel quality, there are also some positive effects. NMIs can act as nucleation sites for heterogenous nucleation, which contributes to grain refinement and improves the microstructure of steel. For example, ALN inclusions serve as nucleation sites in Al killed steel producing fine grained structure [27]. Same process is carried out by adding master alloys to steel which contain inoculant and it is known as inoculation treatment. This process is considered to be a cheap and efficient way to produce small equiaxed grains during the casting process [28]. In addition, some inclusions improve the machinability of steel such as sulfide inclusions including MnS which acts as crack inhibitor and improves steel toughness. It was found that an increased sulfide level results in prolonging the tool life. Nevertheless, this was at the expense of reducing corrosion resistance of steel [29].

2.1.1. Treatment of NMIs

Treatment of NMIs usually follows one of two paths or both: removing of NMIs or modification of NMIs. In the former approach, the number of inclusions is reduced. In the latter, inclusions are made less harmful by controlling their compositions and morphologies.

Steel cleanliness is not controlled in a particular stage of the steelmaking process; instead, almost all process stages contribute to cleanliness control, including tundish, ladle, and casting practices. Treating NMIs does not only mean reducing inclusion number density in steel but also controlling their size, spatial distribution, and avoiding critical sizes that are harmful to the steel. However, there is no specific route for producing UCS. Nevertheless, the cleanliness of steel is usually determined in the secondary metallurgy and casting stages. For example, ladle furnace (LF), RH degasser or Vacuum Degassing (VD) through controlled purging or specific selection of slag and refractory compositions and specific optimization in the casting process (tundish installations, mold control, SEN properties); also tertiary metallurgy is another route for improving the cleanliness of steel [30]. As for the remelting, it is an optional route that is usually applied on special alloys to remove tramp elements that are impossible to remove with oxygen blowing (e.g., Cu, Ni, Mo, Sn, As, Sb).
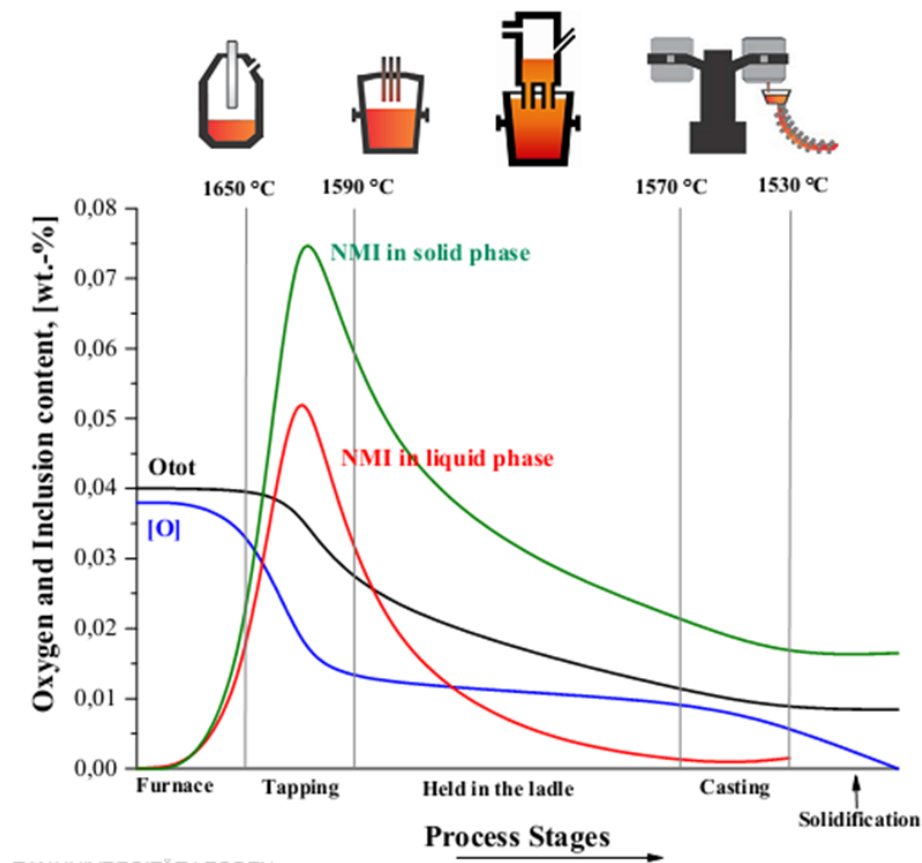
Figure 2.2. Oxygen and inclusions content in liquid steel throughout the production stages.

In steel production, the stage most responsible for the creation of NMIs is the tapping of liquid steel from the furnace (EAF or BOF) to a ladle, as shown in Figure 2.2. In this stage, liquid steel is exposed to air, and thus, the subsequent process of deoxidation usually uses aluminum in the ladle. Oxidation of tramp elements in liquid steel occurs, especially for those of high oxygen affinity (e.g., Al),. In the case of Al-killed steel, Al_2O_3 particles are the most dominant inclusion type in the melt after the treatment. In the case of Mn-Si treatment, higher fractions of Mn-Si inclusions exist in the melt. Major consideration should be attributed to the casting process to maintain the

cleanliness of steel since there is a possibility of re-contamination of molten steel during casting. Thus, steady-state conditions in the process are essential, for example, the modern advances in monitoring and process control.

The submerged entry nozzle (SEN) is one of the main components of the CC flow control system. SEN is a refractory pipe that conveys liquid steel from the tundish to the mold [31]. Its main function is to prevent the pick-up of oxygen by liquid steel and maintain a stable flow. The refractory material of the SEN should be chemically inert and have high thermal shock resistance and high mechanical and thermal strength. Currently, SENs are mainly made of alumina-carbon refractories, while fused silica and zirconia carbon are used to a less extent [32]. An optimized SEN helps controlling the dynamic behavior of NMIs by adjusting the flow pattern so that the inclusions float to the surface, and be picked up by the slag. While if the flow pattern is not optimized, these inclusions will be trapped in the steel [33]. One of the main concerns related to the SEN is the buildup of NMIs on its inner surface, causing the reduction of its cross-section area. If the flow passage for steel from the tundish to the mold is reduced in size, the fluid flow is disturbed. This will affect the quality of the produced steel, reduce productivity, and lead to the evolution of surface defects. This phenomenon is called clogging. Clogging results in disturbing the flow pattern of liquid steel, leading to an uneven heat distribution which results in "the entrapment of inclusions onto the solidified steel shell, the entrainment of top liquid slag, and even breakouts" [34,35]. The service life of SEN is significantly affected by clogging. Moreover, clogging reduces the net casting throughput and results in additional costs [36]. The mechanism of clogging is illustrated in Figure 2.3.

There are four types of clogging based on the origin of the built-up material [37,38]. These are deoxidation products, solidified steel, iron oxides arising from reoxidation, and reaction products. Deoxidation products are usually alumina, zirconia, or titania. They are found in the form of a sintered network. Solid steel build-up when the heat transfer from the stream is high while the superheating is low, which causes steel to be frozen within the nozzle. This is most likely to happen at the beginning of the cast when the nozzle preheat is insufficient. Sometimes, deoxidation products are found to be deposited on the SEN wall in the form of films instead of a sintering network. This is attributed to the reaction of deoxidants with one of the following: air drawn to the nozzle due to pores in the nozzle and negative pressure, or oxygen generated from silica refractory decomposition [39]. However, the primary cause of clogging is the already present inclusions and particularly alumina inclusions. "It has been reported that around 10% of alumina inclusions that leave the tundish adhere to the SEN walls" [34].

Numerous studies have been carried out to describe the mechanism of clogging within the SEN [40,41]. Due to air leakage or air diffusion through the refractory, oxygen activity at the SEN wall rises, leading to the oxidation of soluble Al into alumina. In the case of a redox reaction, SiO_2, Na_2O, and K_2O react with carbon from the refractory forming SiO, Na, K, and CO. When SiO and CO reach the liquid steel, they increase the oxygen activity which results in the oxidation of [Al] whereas Si and C dissolve in the liquid steel. First, a layer of alumina is formed on the refractory wall, which serves as a thermodynamically ideal substrate for the deposition of more inclusions from the liquid steel. Alumina inclusions are then accumulated on this substrate and after adhering to the refractory, the inclusion layers begin to sinter [42].

Clogging can be reduced by pumping a stopper rod into and out of the nozzle and continuing the casting series in this way, without changing the nozzle, as illustrated in Figure 2.4 [43]. Another method is argon injection. Argon is injected through the nozzle wall from a gas sleeve in the tundish nozzle or from the stopper rod into the steel stream with a typical rate of 5 liter/minute (see Figure 2.5.) [44]. Ar forms a film on the nozzle wall that prevents deoxidation products from contacting the wall. Moreover, Ar bubbles adsorb deoxidation products at their surfaces to decrease the inclusion number density. Clogging can also be prevented by Ca treatment. It was suggested that the SEN flow properties are improved when the Ca/Al ratio in the tundish exceeds 0.115 [45]. Ca reacts with the present alumina inclusions within liquid steel to form softer calcium aluminates [46–48].
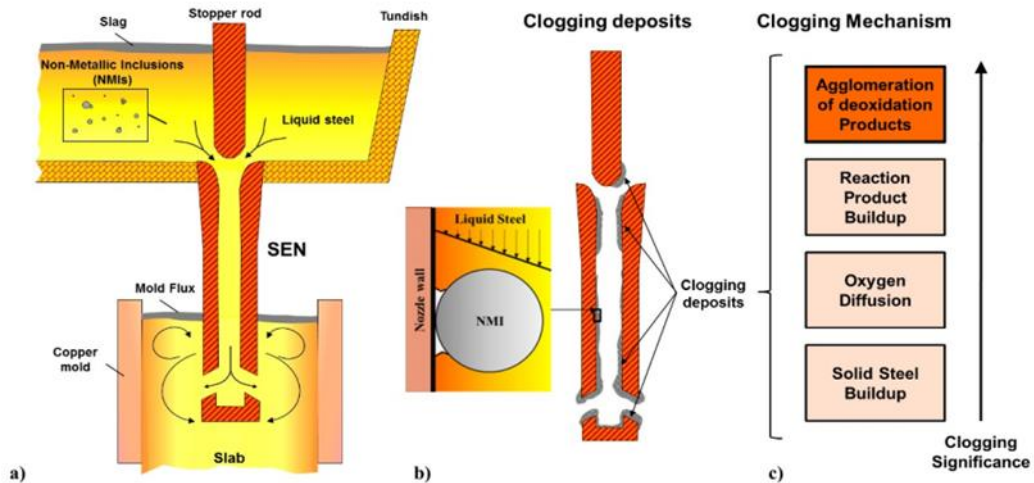
Figure 2.3. Schematic representation of clogging mechanism inside the SEN [36].
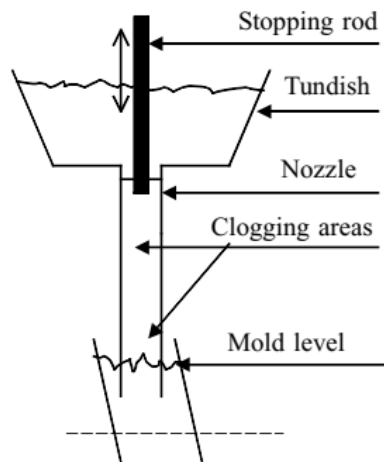
Figure 2.4. Schematic view of pumping the stopping rod into the SEN to reduce the effect of clogging [43].
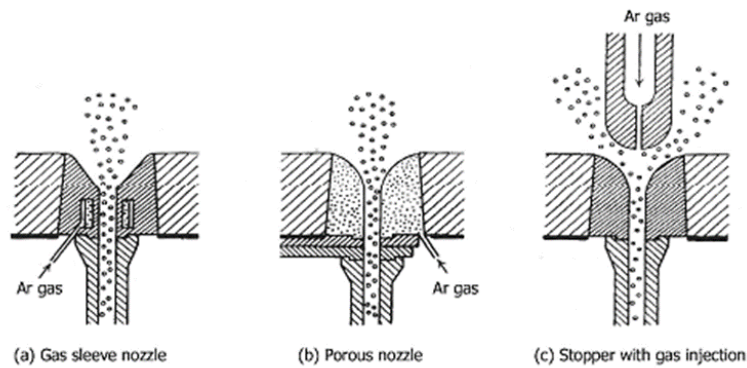
Figure 2.5. Ar injection from (a) gas sleeve, (b) porous nozzle, and (c) stopper rod [44].

2.2. Interactions between particles bound to liquid/gas interface

As mentioned before, argon is introduced to the tundish or the SEN to remove inclusions and reduce nozzle clogging by trapping the particles on the bubble surface. Particles floating on the surface of liquid steel or attached to the bubble surface tend to attract each other and form clusters which will deteriorate steel's mechanical properties if they remain in the steel. The attraction force between these particles is mainly attributed to the capillary interaction which is due to the interface deformation caused by the floatation of the particles on the liquid surface. The origin of the capillary interaction is the overlap of the perturbated liquid interface introduced by the attached particles (floating or partially immersed) [49]. Under the capillary attraction, small inclusions tend to agglomerate to form big clusters. However, the big clusters are more influenced by the adjacent turbulent flow which results in their detachment from the bubble surface during argon purging [50]. Moreover, a big cluster could be deposited on the nozzle wall and become more harmful if it is trapped in the solidified steel. Thus, A better understanding of the behavior of the inclusions on the bubble surface is essential information that could serve in the development of UCS production.

2.2.1. Lateral capillary interaction

Interactions between floating particles attached to fluids interface can be divided into four main categories: (1) capillary interactions; (2) electrostatic interactions for charged colloids; (3) Van der Waals interactions; and (4) interactions due to thermal energy. In most cases all these forces are too small compared to capillary and electrostatic interactions. However, In the case of particles floating on liquid steel surface, electrostatic interactions are eliminated, since they cannot propagate in liquid metal. Therefore, capillary interaction dominates over all other interactions. Thus, to understand the behavior of alumina inclusions floating on the surface of liquid steel, the theory of lateral capillary interaction is studied. Small particles floating on the surface of a liquid within a gaseous atmosphere are subjected to several forces. These forces influence their behavior towards each other as well as the shape of the surrounding interface. These forces are caused by the surface energy of the particle with respect to both the liquid and gas phases and gravity. Describing the shape of the interface (meniscus) surrounding the floating particle is

achieved by solving the Young-Laplace equation, which is a second-order nonlinear differential equation that can be solved numerically [51].

2.2.2. Surface tension

An important parameter in the Young-Laplace equation is the surface tension which is the elastic tendency of a fluid to shrink into the minimum surface area possible [52]. Surface tension is caused by the cohesive forces between fluid molecules (liquid or gas).There are two mechanisms of surface tension. The first mechanism is responsible for the liquid contraction. In this mechanism, Liquid molecules in bulk are attracted to each other in all directions resulting in a net force of zero. However, on the liquid surface, the net force acting on the top molecules is not zero. While the surface molecules are subjected to an attraction force from their neighboring molecules to the bottom pulling them downwards, there are no upper molecules to pull them upwards except for the gas molecules which pose a relatively negligible force. Therefore, the surface molecules are pulled inward. The result of this force is that the outer surface of liquid resists any deformation of the interface and acts as an elastic membrane [53]. This explains the phenomenon of some objects and insects, which are much denser than water, however, being able to float on the water surface. The second mechanism explains the tangential force parallel to the liquid surface. The pressure (p_o) applied on a body in a bulk liquid or gas is the same regardless to the orientation of measuring it. However, near the interface, due to the difference in densities between the liquid and gaseous phases, the pressure acting parallel to the interface (p_t) becomes negative and a tangential tensile stress arises [54]. This mechanism is illustrated in Figure 2.6. Surface tension is expressed by the Greek letter σ and is measured in force per unit length (N/m).
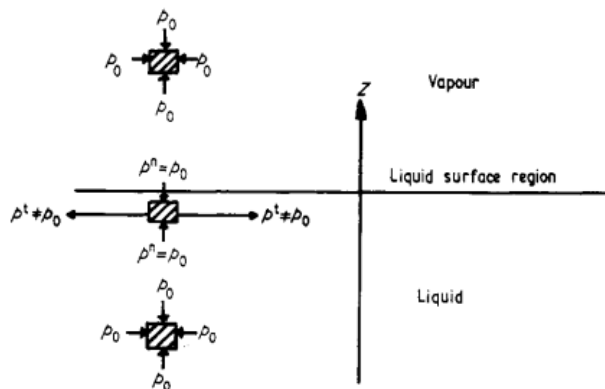
Figure 2.6. The tangential surface tension acting near the liquid-gas interface [54].

Surface tension is responsible for the meniscus shape around floating particles. A meniscus is defined as the curve formed by a liquid against a floating particle or against the container wall. Due to the adhesive forces between the liquid and the floating particle, the liquid molecules tend to stick to the particle surface (or the container wall). Thus, they attach to the particle surface above the liquid surface level, and due to the cohesive forces between water molecules, they attract each other pulling each other upwards and form the meniscus shape. This occurs when the attraction force between liquid molecules and the particle surface (adhesive force) is stronger than the cohesive forces between the liquid molecules. In such case, the floating particle is said

to be hydrophilic. Alternatively, if the cohesive forces are larger than the adhesive forces, the meniscus shape is convex and shaping below the liquid surface level.
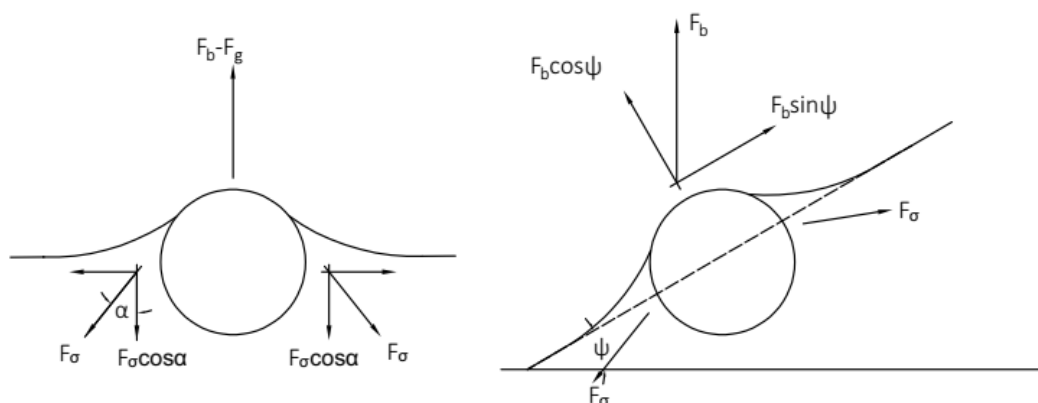
Figure 2.7. Sketch of lateral capillary interaction showing a cross-section of a particle floating on a liquid surface. On the left side, a horizontal interface. On the right side, an inclined interface when a particle is within the capillary range of another. F_b is the buoyant force, F_σ is the surface tension force, and F_g is the gravitational force.

2.2.3. Gravitational component

Besides surface tension, there is the gravitational force which unfolds in the form of two opposite forces: weight, and buoyancy. The weight of the particle pushes it downwards, while the buoyancy arising from the difference between the fluids and the particle density pulls the particles upwards. It is worth noting that the buoyancy force is exerted on the floating particle by both the liquid (on the submerged part) and the gas (on the floating part), however, if the floating particle has high density the gaseous contribution of buoyancy can be neglected. A balance is set up between these forces thanks to the surface tension factor and a state of equilibrium is established. The physical origin of the attraction between floating particles at the fluid-fluid interface can be understood when observing the behavior of bubbles trapped at the interface between liquid and gas, as in the case of sparkling water. When poured sparkling water into a glass container, gas bubbles float to the water surface and tend to move toward each other or drift toward the exterior walls. This phenomenon is called the "Cheerios effect". Due to the meniscus effect caused by the surface tension at the water surface, the interface around the bubble is deformed. As the bubble is buoyant, the net gravitational force acting on it is in the upward direction. However, the bubble cannot simply move upwards as it is constrained to the interface. Instead, it moves upward along the meniscus of the neighboring particle, which means that it moves towards the neighboring particle. In the case of two denser particles, the net force applied on a particle would be downward; however, it does not sink because of surface tension. Instead, it moves along the curved meniscus of the other particle, which is curved downward. Therefore, in-situ observation of these particles shows an obvious attraction between each other [55].

The phenomenon of particles floating on the interface of fluids and attracting each other forming clusters, is called "lateral capillary interaction". It originates from the deformation of the liquid

surface around the particles, which should be flat in the absence of these particles. This deformation makes the gravitational potential of the particles decrease as they approach each other. The larger the surface deformation, the greater the attraction force between the particles. Capillary interaction is also observed in the case of partially immersed particles in a liquid layer. In this case, the physical origin of the capillary interaction is the wetting properties of the particle surface rather than the gravitational potential.

Lateral capillary interaction is distinguished from the well-known "capillary bridges" phenomenon in that the capillary bridges forces act normal to the 2-fluid interface while lateral capillary forces act tangentially to the interface [56].

To quantitatively describe the capillary attraction force between floating particles, several models have been developed [6,11,57]. Nicolson developed a simple superposition model to describe the capillary interaction between two floating bubbles [6]. The capillary interaction energy between two floating particles was assumed to be coinciding with the resultant gravitational force on particles (including buoyancy and weight). Nicolson assumed that for a single particle floating on a liquid surface, two opposite vertical forces act on it: the vertical component of the surface tension force and the buoyancy force arising from the immersed part of the particle. A balance is maintained between these forces keeping the particle in place. In the case of two particles lying within the capillary range, the interface of one particle becomes no longer horizontal but inclined at an angle ψ. This drives the particle to arise along the curved interface of the other particle by the effect of buoyancy and thus, they approach each other. This occurs when the floating particle is light, and the buoyancy force predominates over the weight of the particle. Accordingly, the angle ψ is positive. If the particle is heavy, the weight force predominates over the buoyancy force and the value of ψ is negative. In the later case, two particles will approach each other drived by the gravitational force pulling them downwards, thus, they will tend to slide over the negative meniscus slope [7].

Nicolson used superposition approximation. The meniscus profile between two approaching particles was assumed to be a superposition of the profiles around two single separate bubbles, each of them having rotational symmetry based on the assumption that the field of a particle does not distort the field of neighboring particle and both fields can be added linearly at any point. The Laplace equation of capillarity was used to describe the meniscus profile. This model (superposition approximation) is only applicable when the meniscus slope is small, and thus, the Laplace equation can be linearized. To meet the invariant contact line, the superposition model is limited to large particle separation compared to particle size.

In Nicolson's model, only the gravitational component of the lateral capillary force was considered. Later, Kralchevsky et al. developed two models to calculate the energy and force of capillary interaction for two spherical particles partially immersed in a liquid layer on a horizontal substrate and two particles attached to an air/water interface. The numerical expressions developed by them were obtained for the case when the slope of the deformed meniscus is small, which is the most common experimental situation. Instead of using superposition approximation as in Nicolson's model, they solved the linearized Laplace equation in bipolar coordinates, which describe the interaction between particles at small interparticle distance more precisely [58]. They introduced the term "grand thermodynamic potential" of the system (W), which included the

gravitational potential contribution as well as the meniscus and wetting surface energies contributions [7]. They estimated the factors affecting this force to be the particle size, surface tension, density, , and contact angle. The analogy between the interfacial deformations and two-dimensional electrostatic potential leads to the term "capillary charge" (Q) to describe the interfacial deformation, which can be positive or negative as well. Contrary to the electrostatics, in the case of capillary interaction, like charges attract each other while dissimilar charges repel. Q is given by equation (2.1).

$$Q_k = r_k sin\psi_k \tag{2.1}$$

Where r_k is the three-phase contact line radius and ψ_k is the angle characterizing the slope of the contact line (see Figure 2.8).
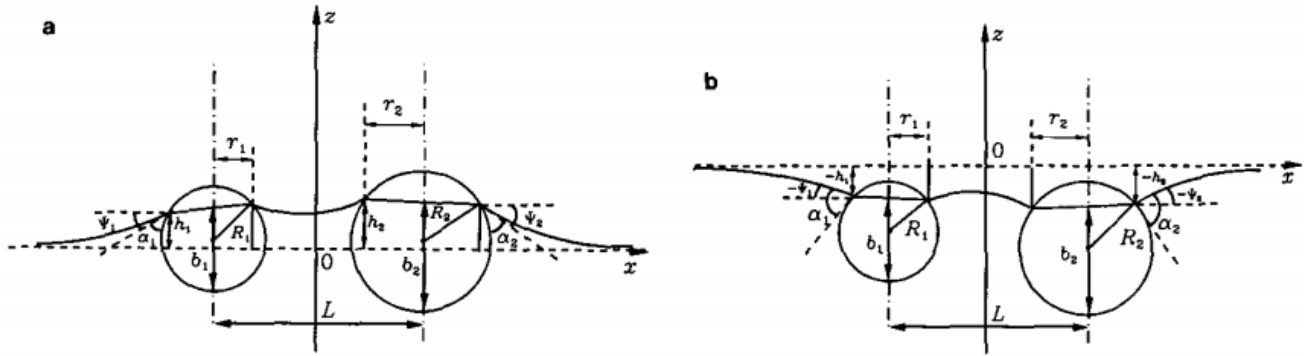
Figure 2.8. Sketch of the capillary meniscus formed around two spherical particles of radii R_1, R_2 and a distance L. (a) light particles. (b) heavy particles. ψ_k is the slope angle of the contact line of particle k, h_k is the mean elevation of the contact line for particle k, r_k is the contact line radius of particle k, b_k is the immersion depth of particle k, α_k is the contact angle of particle k [7].

Paunov et al. [7] derived a theoretical expression for the lateral capillary force between floating particles based on a linearized version of the Laplace equation. Laplace equation is given as:

$$\nabla_{II} \cdot \left(\frac{\nabla_{II}\xi}{\sqrt{1 + |\nabla_{II}\xi|^2}} \right) = [P_{II}(\xi) - P_I(\xi)]/\sigma \tag{2.2}$$

$$\nabla_{II} = e_x \frac{\partial}{\partial x} + e_y \frac{\partial}{\partial y} \tag{2.3}$$

Where $\xi(x, y)$ is the equation to describe the deformed fluid interface, ∇_{II} is the two-dimensional gradient operator in the plane xy, P_I and P_{II} are the pressures at the two sides of the interface which depend on ξ because of the curved surface induced capillary pressure. This equation is linearized based on the assumption that the slope of the meniscus around the particle is small enough that $|\nabla_{II}\xi|^2 \ll 1$. Equation (2.2) is thus reduced to:

13

$$\nabla_{II}^2 \xi = q^2 \xi \tag{2.4}$$

Where q^{-1} is a characteristic capillary length which determines the range of action of the lateral capillary force and is given by equation (2.5).

$$q^{-1} = \left[\frac{\sigma}{(\rho_I - \rho_{II})g}\right]^{1/2} \tag{2.5}$$

Where ρ_I and ρ_{II} are the densities of the liquid and the gaseous phases respectively, and g is the gravitational acceleration. The free energy of the system (W) was represented as a superposition of the contributions of gravity (W_g), wetting (W_w), and the meniscus interfacial energy (W_m).

$$W = W_g + W_w + W_m \tag{2.6}$$

The gravitational energy of the particles (W_g) accounts for the weight of the particles, the liquid and the gaseous phases within the capillary range beside their vertical position with respect to the interface at infinity (at a large interparticle distance with respect to the capillary range).

2.2.4. Wetting component

The wetting component (W_w) represents the interface energy of the particle at the area of interface between the particle and the liquid as well as the area of interface between the particle and the gas phase. The wettability of a solid surface by a liquid is quantified by the contact angle via Young's equation if the surface tension is known (equation (2.7). A surface is considered to be hydrophilic if the contact angle with this surface is smaller than 90° and is considered to be hydrophobic if the contact angle is larger than 90° [59]. The contact angle is also experimentally measured by visualization for large particles (~1 mm), while for smaller sizes, other techniques such as freeze fracture, gel trapping, shadow casting, interferometry, and atomic force microscopy are used [60]. In the static state, the contact angle is referred to as the equilibrium contact angle and it is the contact angle calculated by Young's equation.

$$\sigma_{SG} - \sigma_{SL} - \sigma_{GL}cos\alpha_k = 0 \tag{2.7}$$

Where σ_{SG} is the solid-vapor interfacial energy, σ_{SL} is the solid-liquid interfacial energy, σ_{GL} is the vapor-liquid interfacial energy, and α_k is the contact angle. α_k depends on many factors, among which is the heterogeneity of the inclusion particle and its surface roughness. With increasing surface roughness, the contact angle increases in the case of hydrophilic materials and decreases in the case of hydrophobic materials. However, this equation does not account for gravity and surface roughness which affect the value of the contact angle. To take these effects into account, contact angle hysteresis (CAH) must be considered. For the same substrate-liquid-gas combination, a range of contact angles are measured at a constant contact area. The maximum is called advancing contact angle (α_v) and the minimum is called receding contact angle (α_R). These values of contact angle can be observed when the contact line is moving. Between these

14

two dynamic values, rate-dependent dynamic CAH is observed [61]. A more accurate value of equilibrium contact angle can be determined based on the estimated advancing and receding contact angles. The difference between the advancing and receding contact angles is defined as Contact angle hysteresis ($\Delta\alpha_k$).

CAH is an essential parameter that needs to be evaluated to accurately determine the capillary interaction force. For an ideal surface, the contact angle is constant and depends only on the material of the floating object and the two fluid interfaces surrounding this object. However, this is rarely the case. In steel making processes and particularly in CC process, NMIs usually have rough surfaces and heterogeneous chemistries. Due to surface roughness and chemical heterogeneity of the floating inclusions, the value of the contact angle is altered. This alteration does not occur uniformly across the contact line but depending on the pinning of the contact line at some positions introducing a CAH. Three experimental methods are used to measure the CAH. In the first method, a droplet is placed on an inclined plate and then the contact angle is measured when it slides down the plate. In the second method, which is known as the sessile drop method, gas is pumped into and out of a gas bubble to measure the advancing and receding angles respectively. A third method is called Wilhelmy plate method. In this method a surface is lowered and pulled up against a liquid bath to measure the advancing and receding angles respectively [62].

2.2.5. Meniscus component

The meniscus component W_m represents the surface energy of the meniscus area. The magnitude of the capillary interaction increases when the meniscus surface energy within the capillary range decreases. This is explained by the fact that less surface tension allows the floating particle to inflect larger interface deformation. Eventually, asymptotic equations for the energy and force of capillary interaction were derived (equations (2.8), (2.9)). It was found that both the meniscus and the wetting contributions were canceled, and therefore, the gravity contribution was the dominant factor in this equation [57].

$$\Delta W = -2\pi\sigma Q_1 Q_2 K_o(qL), \qquad r_k \ll L \tag{2.8}$$

$$F = \frac{d(\Delta W)}{dL} \tag{2.9}$$

The asymptotic expression for capillary force is then given by:

$$F = 2\pi\sigma Q_1 Q_2 q K_1(qL)[1 + O(q^2 R_K^2)], \quad r_k \ll L \tag{2.10}$$

Where K_1 is the modified Bessel's function of the first order, $O(x)$ is the zero function of approximation and, r_k is the radius of contact line of particle k.
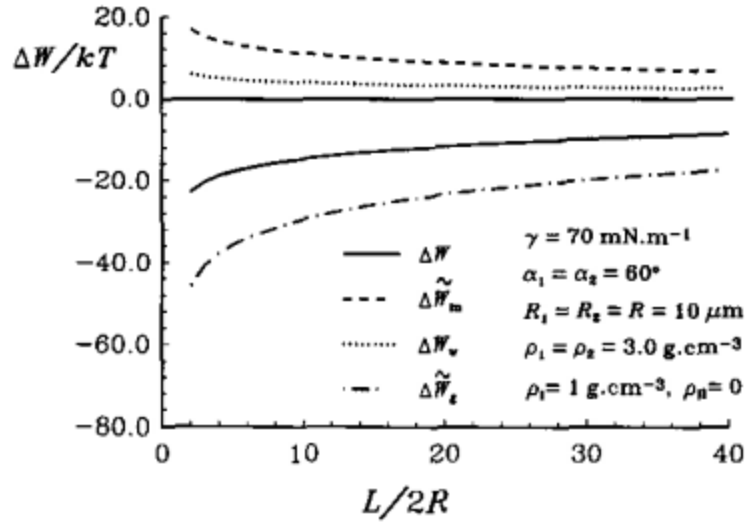
Figure 2.9. The contributions of gravitational, wetting, and meniscus energies to the interaction energy ΔW plotted versus the interparticle distance expressed as $L/2R$ [7]. The total interaction energy is approximately equal to half of the gravitational energy.

By adding the contributions of gravitational, wetting, and meniscus energies it was found that the total interaction energy was approximately equal to half of the gravitational energy. The contributions of these different energies are illustrated in Figure 2.9. All the changes in the contributions are almost linear at large interparticle distance. While the meniscus and the wetting contributions are positive which means that they serve in increasing the interaction energy difference and thus repelling the particles from each other. The gravitational contribution, however, is noticeably larger than the former contributions and serves in decreasing the interaction energy difference and thus the attraction between the particles. Consequently, the net interaction energy difference ΔW is in positive and the attraction force increases exponentially at a small interparticle distance [7].

This model, however, was only applicable to submillimeter particles and small meniscus slopes. Moreover, the calculations showed that the capillary interaction related to the gravitational force between the floating particles of sizes less than 10 µm was negligible (smaller than the thermal energy kT). As a result, this model did not explain the detected attraction force between particles smaller than 10 µm as it only considered the uniform contact line.

2.2.6. Experimental methods for measuring lateral capillary force

While several experimental measurements of the immersed lateral capillary force were carried out [63,64]. Measuring capillary force for floating particles type is more difficult. Velev et al. measured it based on the counterbalance of capillary force by gravitational force in the vicinity of an inclined meniscus using a torsion balance system designed by Dushkin et al. [65] (Figure 2.10). Two pairs of spheres are attached to holders and let to float in a water bath. A center anchor is suspended on a platinum wire. The attraction force between the two couple of spheres creates a

torsion moment. This moment is counterbalanced by the platinum wire. A mirror is attached to the anchor of the balance on which a laser beam is reflected which is used to measure the angle of torsion. The experimental results agreed with the theoretical models within their range of validity. At small interparticle distances, the experimental results deviated from the theoretical expressions, which linearized the contact line.
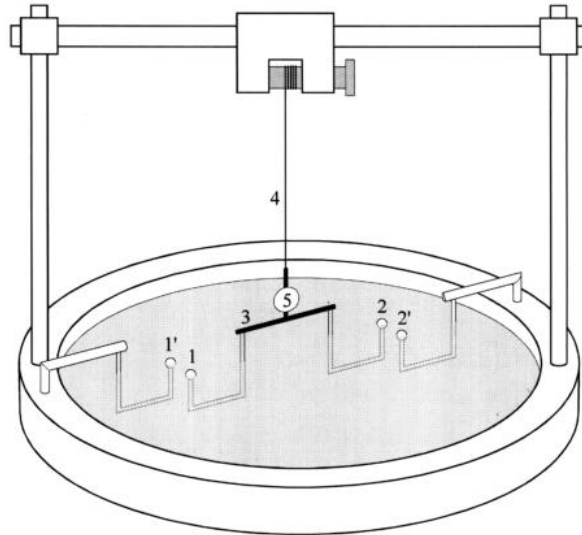
Figure 2.10. Sketch of the torsion balance used by Dushkin et al. to measure the capillary force between two pairs of floating small glass spheres (1,1'-2,2'), 3 is a central anchor, 4 is platinum wire, and 5 is a mirror [65].

Another experimental method was used by Pektov et. al [66]. In this method, the displacement between the approaching floating particles under the effect of capillary force is recorded with respect to time, and by knowing the drag force coefficient, the capillary force can be determined. This method is thus used in our thesis to determine the capillary force acting on floating alumina inclusions at the liquid steel/argon gas interface.

2.2.7. Undulated contact line model

In the previously mentioned models, it was estimated that the capillary interaction between two floating particles at an interface was negligible for particle sizes less than 10 µm [7]. The particles were assumed to have chemical homogeneity and smooth surface. Moreover, the models were only applicable to simple geometries (spheres and cylinders) [65, 66]. However, NMIs, including alumina, are in most cases not limited to these conditions, and their shapes are mostly irregular. Consequently, the uniform contact line model could not explain the strong capillary interactions experimentally observed for particle sizes less than 10 µm. Later Lucassen suggested another type of lateral capillary force [67]. He studied floating particles with irregular "jagged" edges. He proposed that even when the gravitational force is negligible, the contact line can be deformed because it hinges on the irregular-shaped edges of floating particles. Hence, a new model was developed to address the following factors: Chemical heterogeneity, surface roughness, and irregular particle shape [11]. These factors affect the contact line between the particle and the

interface leading to an irregular-shaped contact line (see Figure 2.11). A model was introduced by Danov et al. [11] to explain the recorded strong attraction force between micrometer particles at which the capillary interaction is negligible due to the fact that the particle weight is too small to cause meniscus deformation. Deformation of the meniscus can still occur in case of the presence of electro dipping force [68]. However, even in the case of the absence of electro dipping force, interfacial deformation around floating particles was still recorded. This is attributed to the undulated contact line at the particle surface. This undulation is assumed to occur due to the heterogeneity of the particle surface, which causes the meniscus to be pinned to it. Pinning of a meniscus to topographic or chemical defects from planar surfaces is well known and referred to as non-uniform wetting [10,69]. The unevenly pinned meniscus will lead to distortion of the liquid interface around the particle. Thus, when two particles approach each other, they will rotate with respect to each other to achieve a minimum integral surface area and hence a minimum surface energy. This will result in a lateral force arising between the two particles. The force between particles, in this case, is described as the interaction between capillary 'multipoles' instead of capillary charges. Stamou et al. derived an asymptotic equation for the interaction energy ΔW to describe the capillary interaction between two spherical capillary quadrupoles (QPs) (equation (2.11)) [10].

The role of the particle shape in deforming the contact line was addressed by Loudet et al. for low temperature systems [70]. Monodisperse polystyrene spheres were uniaxially stretched to obtain ellipsoidal shaped samples. The samples were placed at an air-water interface and it was found that they were strongly attracted to each other compared to perfect spheres which did not show such interaction. The contact line around the ellipsoid sample was found to be deformed unevenly. The contact line deformation increased with increasing shape distortion. It was concluded that the role of particle shape had a greater influence on contact line deformation compared to surface roughness [70].
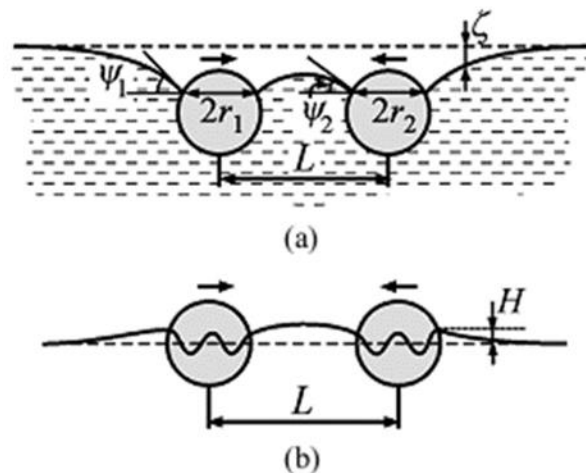
Figure 2.11. Lateral capillary forces between two floating particles. (a) deformation caused by particle weight and buoyancy (normal force) or electro dipping (b) deformation caused by undulated contact line at the particle surface [11].
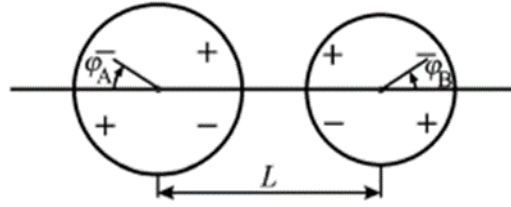
Figure 2.12. Sketch of two particles, "capillary QPs," A and B, separated at a distance L. The signs "+" and "−" symbolize convex and concave local deviations of the contact line from planarity. The φ_A and φ_B denote the angles of rotation of the respective particles with respect to their initial state ($\varphi_A = \varphi_B = 0$) [11].

$$\Delta W(L) \approx -12\pi\sigma H^2 \cos(2\varphi_A - 2\varphi_B)\frac{r_c^4}{L^4} \qquad (L \gg 2r_c) \qquad (2.11)$$

Where L is the distance between the centers of the two particles, H is the contact line undulation amplitude, r_c is the contact line radius, the angles φ_A and φ_B are the angles of rotation around a vertical axis with respect to the respective particle initial state (see Figure 2.12.). It was noted that the floating particles rotate normally with respect to the contact line to achieve minimum capillary interaction energy [67].
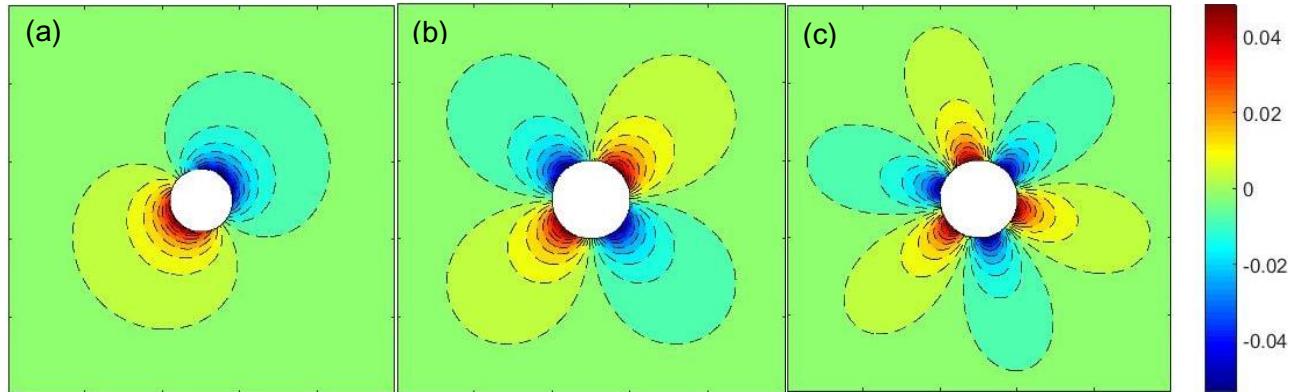
Figure 2.13. Meniscus profile around floating particles in the case of the undulated contact line. (a) DP, (b) QP, and (c) HP. The legend refers to the ratio of the undulation to the particle size. i.e., red and blue mean convex and concave interfaces respectively.

The interaction energy between two capillary QPs was examined experimentally by Brown et al. [71]. Afterwards, Danov et el. derived asymptotic expressions for ΔW for different values of multipoles (charge- QP, DP-QP, QP- HP, etc.) (see Table 2.1) [11]. At a small distance, particle size does not influence the capillary interaction anymore; instead, it is a function of the amplitude of undulation (H) and the running azimuthal angle ($\Delta\varphi$). Moreover, one can see from Figure 2.14. that "the interaction could be either monotonic attraction, or monotonic repulsion, or it is attraction at long distances but repulsion at short distances" [11].

Table 2.1. Asymptotic expressions for $\Delta W(L)$ for some values of n_A and n_B.

Type of interaction	(n_A, n_B)	Interaction energy ΔW for $r_A, r_B \ll L \ll q^{-1}$
Charge- QP	$(0, 2)$	$-\dfrac{\pi}{2}\sigma Q_A H_B \cos\left[2(\varphi_B - \pi)\right]\left(\dfrac{r_B}{L}\right)^2$
Charge- multipole	$(0, n_B)$	$-\dfrac{\pi}{2}\sigma Q_A H_B \cos\left[m_B(\varphi_B - \pi)\right]\left(\dfrac{r_B}{L}\right)^{n_B}$
DP- QP	$(1, 2)$	$4\pi\sigma H_A H_B \cos\left[\varphi_A - 2\varphi_B\right]\dfrac{r_A r_B^2}{L^3}$
QP- QP	$(2, 2)$	$-12\pi\sigma H_A H_B \cos\left[2(\varphi_A - \varphi_B)\right]\dfrac{(r_A r_B)^2}{L^4}$
QP- HP	$(2, 3)$	$24\pi\sigma H_A H_B \cos\left(2\varphi_A - 3\varphi_B\right)\dfrac{r_A^2 r_B^3}{L^5}$
HP- HP	$(3, 3)$	$-60\pi\sigma H_A H_B \cos\left(3\varphi_A - 3\varphi_B\right)\dfrac{r_A^3 r_B^4}{L^6}$
HP- octupole	$(3, 4)$	$120\pi\sigma H_A H_B \cos\left(3\varphi_A - 4\varphi_B\right)\dfrac{r_A^3 r_B^4}{L^7}$
Multipole- multipole	(n_A, n_B)	$-G_o\pi\sigma H_A H_B \cos\left(n_A\varphi_A - n_B\varphi_B\right)\dfrac{r_A^{n_A} r_B^{n_B}}{L^{(n_A+n_B)}}$

Where G_o is a constant independent of L and is given by:

$$G_\circ = \sum_{n=1}^{\min(n_A, n_B)} \frac{2(-1)^{n_A + n_B} n_A! \, n_B!}{(n_A - n)! \, (n_B - n)! \, n! \, (n - 1)!} \tag{2.12}$$

In the undulated model, the letter n refers to the order of multipole interaction. For instance, the term QP is referred to by the expression $n = 2$, and it means that two parts on opposite sides of the meniscus around the floating particle are concave while the other two parts on opposite sides are convex. Similarly, if a particle is said to be a HP, it means that three parts on opposite sides of its meniscus are concave while another three parts are convex and, in this case, $n = 3$. Typical DP, QP, and HP meniscus profiles based on this model are shown in Figure 2.13.

It was noted that for a given amplitude H, ΔW does not depend on r_c which means that the capillary force for a given amplitude and a given multipole will be the same for different multipole radii [11]. Instead, ΔW is strongly dependent on the contact line radius r_k. Additionally, the influence of H_k is significant. H_k is a function of CAH ($\Delta\alpha_k$).
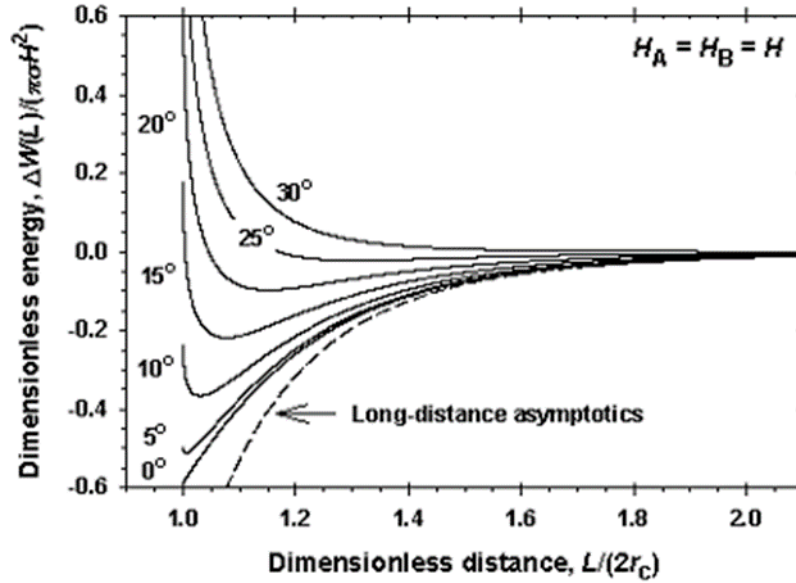
Figure 2.14. Capillary interaction energy between two capillary HPs versus the interparticle distance at different phase angles [11].

2.2.8. Drag Force

Another force acting on the floating alumina particles when they are sliding on the liquid steel surface is the drag force. Drag force is the force acting opposite to the direction of motion of an object moving with respect to a fluid due to the motion of the fluid [72]. The magnitude of this force is a function of the velocity of the floating particles with respect to the fluid. It also depends on the properties of the fluid and the size and shape of the object. Drag force is proportional to the velocity of the moving object in the case of low-speed flow and the squared velocity in the case of high-speed flow. Reynold's number indicates whether the flow is high or low speed [73]. The general form of the drag force equation is shown in equation (2.13):

$$F_D = {}^1\!/_2\, \rho v^2 C_o A \tag{2.13}$$

Where F_D is the drag force, ρ is the density of the fluid (liquid steel in our case), v is the velocity of the particle relative to the fluid, C_o is the drag coefficient, and A is the cross-sectional area. For very small particles such as alumina inclusions in steel, drag force is proportional only to the velocity and it is given by Stoke's law:

$$F_D = 6\pi R \mu v \tag{2.14}$$

Where μ is the viscosity of the fluid. The drag force of a floating particle on a liquid surface is given by:

$$F_D = 6\pi \mu R f\left(\frac{b}{R}, \kappa\right) v \tag{2.15}$$

Where f is the translational drag resistance coefficient for a particle floating on the interface and it is a function of $\frac{b}{R}$. To determine the drag coefficient f, Pektov et al. used ''Random middle deviation of squares (RMDS)'' [66]. b is the immersion depth into liquid, $\kappa = \mu_w/\mu$ is the viscosity ratio where μ_w is the viscosity of liquid, and the limit $\frac{b}{R} \to \pm \infty$ corresponds to the familiar resistance of a particle in an infinite liquid of either adjoining phase. Danov et el. used this latter assumption to calculate the drag coefficient [74]. After solving a Fredholm equation of the second kind, Dani et el. Determined f as a function of $\frac{b}{R}$ using the following equation [75]:

$$f\left(\frac{b}{R}\right) = \frac{\sqrt{2}i(sin\eta_o)^3}{3\pi} \int_{-i\infty}^{i\infty} \left(s^2 - \frac{1}{4}\right) X(s) \frac{\left(ssin(2\eta_o)+\frac{3}{2}sin(2\eta_o)s\right)}{cos\,(\eta_o s)\left(cos(2\eta_o s)+cos(2\eta_o)\right)}ds \qquad (2.16)$$

Where η_o is a spatial variable in a toroidal coordinate system determined by the immersion depth of the sphere and it is related to a and d as given by:

$$\cos(\eta_o) = 1 - \frac{b}{R} \qquad (2.17)$$

s is an imaginary transform variable used in solving a Mehler-Fock transform. The derivations of these equations can be found elsewhere [75].

Chapter three: Materials and methods

In this chapter, the experimental procedure for examining the behavior of alumina inclusions at the argon/liquid steel interface is described. First, the sample was prepared using a resistance vertical tube furnace. Then the sample was cut into discs of suitable sizes for the CSLM observation. For five steel samples, three of them were used in the CSLM *in-situ* observation, while the other two were used in chemical extraction for 3D shape analysis of the inclusions.

3.1. Sample preparation

3.1.1. Raw materials

Prior to the *in-situ* CSLM observation, the steel sample containing Al_2O_3 inclusions was prepared. The raw materials used for the sample are pure iron flakes, aluminum, and ferric oxide (Fe_2O_3) powder brand "Thermo scientific" of concentration 98%. Al foil brand Pro-analysi of thickness 0.3 mm and width 30 mm was used. The amount of Al was calculated with respect to the input iron to obtain aluminum content of 500 ppm in the sample. The pure iron flakes are brand Chempur, purity 99.9%. Thus, impurities should be minimized. Ferric oxide was the source of oxygen needed to form alumina inclusions. The exact amounts of input materials are given in Table .

The aluminum content was determined by trial and error. Three attempts were carried out. In the first trial, the targeted Al content was 1000 ppm. However, in the CSLM observation, the liquid steel surface was completely covered with large dendritic clusters of alumina which formed a continuous network above the liquid steel surface, and therefore, the recording of micro alumina inclusions was not possible. The surface of liquid steel sample at Al content of 1000 ppm is shown in Figure 3.1.. In the second trial the aluminum input mass was reduced to achieve an Al content of 300 ppm. The CSLM observation on this sample showed that the surface of liquid steel was almost free of any inclusions and therefore, again the recording of alumina inclusions collisions was not possible. Finally, in the last trial the alumina content was set to 500 ppm. Only at this Al content the amount of alumina inclusions was sufficient for the rising of an adequate number of inclusions to the surface and on the other hand was not too large to cover most of the surface with large dendritic clusters of inclusions.

Table 3.1. Material input for the sample preparation in the vertical tube furnace.

Material	Mass [g]
Iron	51
Aluminum	0.025
Ferric oxide (Fe_2O_3)	0.0208
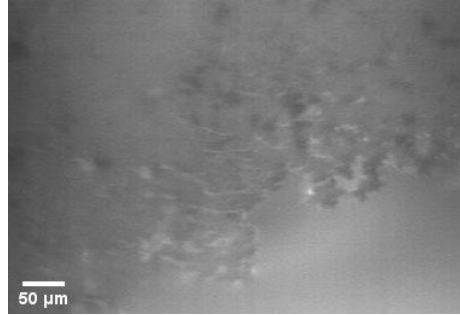
Figure 3.1. Image of the surface of liquid steel sample at Al content of 1000 ppm taken from the CSLM observation. The liquid surface is mostly covered in networks of alumina dendrites.

3.1.2. Vertical tube furnace

The steel sample was prepared using a vertical tube GERO furnace (type: HTRV 100-250/18) in the department of Material science of KU Leuven. A schematic representation of the furnace is given in Figure 3.2.. The vertical tube furnace uses $MoSi_2$ as the heating element, and it is used for lab-scale metallurgical experiments. "The furnace tube is made of sintered Al_2O_3, with dimensions of 80 mm inside diameter, 90 mm outside diameter, and 1000 mm height" [76]. The temperature inside the furnace is measured by a thermocouple positioned below the crucible outside the tube. The safety working temperature is from 1000 ℃ to 1700 ℃. Argon and CO gas tubes are connected to the furnace tube. Ar is either introduced to the furnace tube directly to flush or is led first through a Mg furnace at 500 ℃ to get rid of oxygen before being introduced to the tube furnace. Since oxygen reacts with Mg at that temperature according to equation (3.1).

$$2Mg_{(s)} + O_{2(g)} \rightarrow 2MgO_{(s)} \tag{3.1}$$

The role of argon is to maintain an inert atmosphere inside the furnace to prevent the oxidation of steel. CO can also be introduced into the furnace to further reduce the oxygen partial pressure (PO_2) level. The input materials are inserted at the bottom of the furnace inside an alumina crucible. The crucible is placed inside another larger protective alumina crucible, and this setup is placed on a supporting alumina tube. There are five holes on the top flange, four of them are for adding material or stirring, and one is for observing the melting process. Before heating up the furnace, a quartz tube is fitted into a rubber stopper and inserted into one of the holes. A syringe is connected to the top end of the quartz tube using a soft silicone tube. This syringe is used to suck the molten steel out of the furnace. Another quartz tube is positioned in another hole and is used to add alloying elements (in this case, aluminum) into the furnace. An alumina rod is placed into another hole and is used to stir the melt inside the furnace. Initially, both the quartz tubes and the alumina rod are placed at a high position where the temperature is low. A programmable PID-controller controls the temperature of the furnace.

24
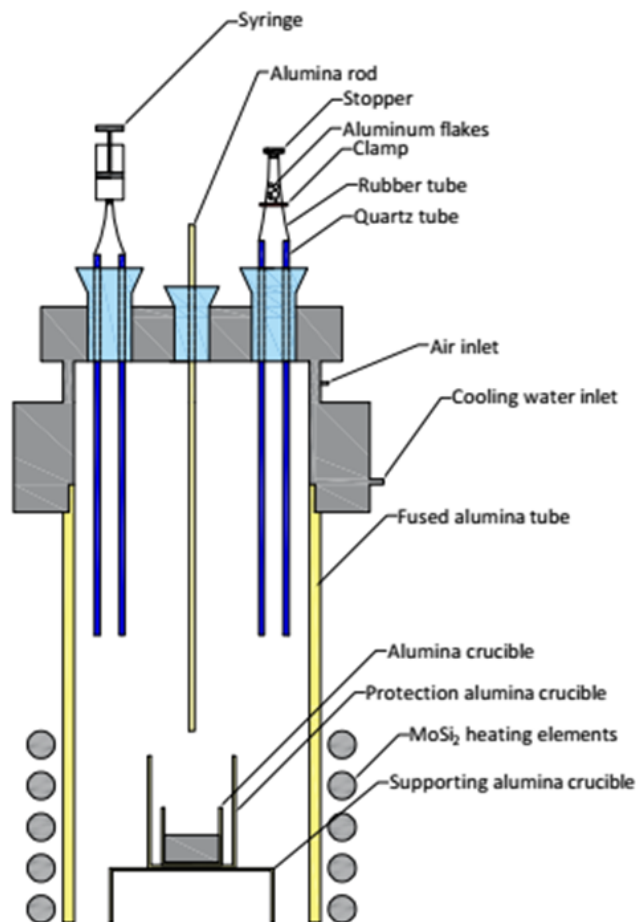
Figure 3.2. Schematic drawing for the vertical tube furnace.

3.1.3. Procedure

First, the raw materials except aluminum were placed inside an alumina crucible. The dimensions of this alumina crucible are 3 cm inner diameter, 3.5 cm outer diameter, and 5 cm height. The crucible was placed inside the tube furnace. Al was stored inside a soft silicone tube sealed with a clamp and connected to a quartz tube inserted into the furnace through one of the holes. The sample was heated up to 1600 ^{o}C with a heating rate of 5 ^{o}C/min, and the furnace was held at this temperature for 30 minutes before adding Al through the quartz tube. Al is added by the quartz tube which is lowered into the high temperature zone on top of the molten steel. The tubing clamp was opened to release the Al grains through the tube and then into the crucible. Afterwards, the quartz tube was removed from the furnace. Aluminum was not added at the beginning of the melting process since it would react with oxygen promptly due to its higher oxygen affinity. As a result, the generated alumina inclusions would float to the top of the melt surface and agglomerate forming big clusters and eventually a slag layer, leaving no more micro-sized alumina inclusions within the sample. After adding aluminum for 30 seconds, the melt was constantly stirred using an alumina rod to ensure a uniform distribution of aluminum. The molten steel was sucked using the syringe at the top end of the other quartz tube three minutes after stirring, followed by a quick

quench into the water. The procedure was carried out carefully to ensure that the atmosphere of the furnace did not change throughout the experiment period. A PO_2 sensor was connected to the furnace and was checked frequently. PO_2 was maintained below 1×10^{-20} ppm throughout the whole process.

3.2. Morphology analysis by chemical extraction

For more precise characterization of the alumina inclusions in steel, a morphology investigation of the inclusions was carried out using chemical extraction of inclusions from steel samples. Previous studies [76] have shown that three-dimensional (3D) investigation methods are more reliable regarding the size and morphology of NMIs compared to conventional two-dimensional (2D) investigations on a polished cross-section of metal samples [77].

To obtain 2D images of the inclusions, first, the steel rod produced by GERO furnace was cut into small disks with dimensions of around 4 mm diameter and from 4 to 8 mm height using an abrasive cutting machine. The disks were then prepared for polishing by mounting them in resin to provide convenient handling and protect the specimen edges. The specimens were then grinded to generate an initial flat surface which could be further grinded and polished to obtain a mirror-polished surface. Wet grinding was carried out using 80, 220, 400, 800, 1200, and 4000 mesh sandpaper and finally suspended abrasives on a rotating disk. When the surface of the specimen was free of any cutting marks and mirror polished it was then examined by SEM.

To obtain 3D images, chemical extraction was carried out on steel specimens. The first step was choosing the most suitable extraction method. Several techniques were investigated [77,78]. Basically, there are two major methods of extraction, which are chemical extraction using acid or halogen alcohols, and electrolytic extraction. In this work, chemical extraction by HCl was considered following the experimental method provided in reference [79]. A steel sample of around 5 g mass was cut from the steel rod prepared by GERO furnace. The sample was washed by acetone to clean the surface, then it was dissolved into a 100 ml aqueous solution of hydrochloric acid-37% (1:1) and 10 ml of HNO_3 (1:1) under heating (100°C). After approximately 3 hours, all iron had dissolved, and the hot iron solution was vacuum filtered over a Nuclepore membrane with pores of 0.2 μm to separate acid soluble and insoluble fractions. The residue was washed alternately with a hot aqueous solution of hydrochloric acid-37% (1:25) and distilled water five times each. The washing should ensure the removal of all iron salts. The Nuclepore membrane was used because of its resistance to acid and its flat surface that facilitates investigation by scanning electron microscopy (SEM).

Figure 3.3. SEM used in the project. Model Philips XL 30 FEG.

The inclusions collected on the Nuclepore membrane were analyzed using the scanning electron microscope (SEM) located in the department of material science of KU Leuven. The model of the microscope is Philips XL 30 FEG which is a Dual Beam SEM/FIB for nanoscale characterization and magnification up to 1,000,000 X. The advantage of SEM is that it uses a very fine, sharply focused electron beam which allows it to provide high accuracy and fast measurements of the size, morphology, and composition of the given samples [76]. The images are generated based on the concept of back scattered electrons (BSEs) which can be used to determine the chemical composition of the sample as well. The details of SEM and the concept of BSE can be found elsewhere [80–82].

3.3. CSLM *in-situ* observation

The confocal laser scanning microscope (CSLM) is a reliable tool used for *In-situ* observation at high temperatures up to 1700 °C with very good quality. CSLM is developed by photonic imaging technology. It has numerous applications in the fields of biology, semiconductor device technology, fluorescence imaging, and material science. "Confocal means that the image is collected from a focal plane only, and any noise resulting from the sample thickness is removed optically" [83]. The microscope uses a laser instead of white light. The advantage of using laser is that "the images are acquired point-by-point under localized laser excitation" [83] instead of illuminating the entire sample. Nevertheless, point-by-point is relatively slow (only a few images per second). Figure 3.4. illustrates the basic principle of the confocal microscope. First the pinhole is illuminated by the He-Ne laser, then the light emerging from the pinhole passes through a modulate beam splitter and is focused by a lens on the spot of the focal plane where the sample is normally placed. Only the light reflected from the spot is reflected while the rest is blocked by

the sensor pinhole and does not reach the sensor. The light coming from the spot is partly reflected by the beam splitter towards the pinhole in front of the charge coupled device (CCD) image sensor [84]. Thus, the image is produced from the fluorescence immitted by the sample after irradiation with the laser beam [83]. The advantage of using the pinhole is that it minimizes the optical pollution by eliminating the out-of-focus light and collecting information from the focal plane only, thus, providing high-resolution images. Moreover, the maximum light intensity only occurs for the focusing points, unlike in the case of conventional microscopy [85]. However, this also means that a small range of the vertical length from the objective lens gives images of sharp edges beyond which the resolution drops drastically.

Associated to the microscope is a small gastight ellipsoidal heating chamber in which the sample is positioned. A 1.5 kW halogen lamp is positioned in the lower focal point of the chamber. The inner wall is plated with gold that reflects the light to the other focus point where the observed sample is positioned. This heating system has a heating rate up to 300 $^{\circ}$C/min. The sample is positioned on the top of a type B thermocouple. The thermocouple is connected to a PID controller that controls the temperature of the sample. Since the thermocouple lies a few millimeters below the upper confocal point, the temperature detected by it is slightly less than the actual temperature of the sample. This small deviation is corrected by calibration of the proportional-integral-derivative (PID) controller. High-purity argon gas is purged into the chamber prior to starting the experiment to ensure a neutral atmosphere inside the chamber and to prevent oxidation of the sample. Additionally, an oxygen sensor is connected to the chamber to continuously measure the oxygen content throughout the experiment. A schematic view of the CSLM is given in Figure 3.4. [8].

In-situ observation of alumina inclusions at the interface between liquid steel and argon gas using the CSLM was first performed by Yin et al. [8]. In this thesis, the *in-situ* observation of alumina inclusions was carried out using a high temperature CSLM-IIF (1LM21H-SVF17SP) located in the department of material science at KU Leuven. Thanks to confocal optics and He-Ne laser (632.8 nm), this microscope can observe samples at elevated temperatures with high resolutions. The confocal lens provides high resolution, however, on a short range compared to other optical lenses. The laser provides a high illumination density needed to observe the sample surface at high thermal radiation. It also provides real-time observation at a maximum video rate of NTSC - 30 fps. The images extracted from the observation process consist of 640 $\times$ 480 pixels with a resolution of 0.7 μm (10X objective lens).
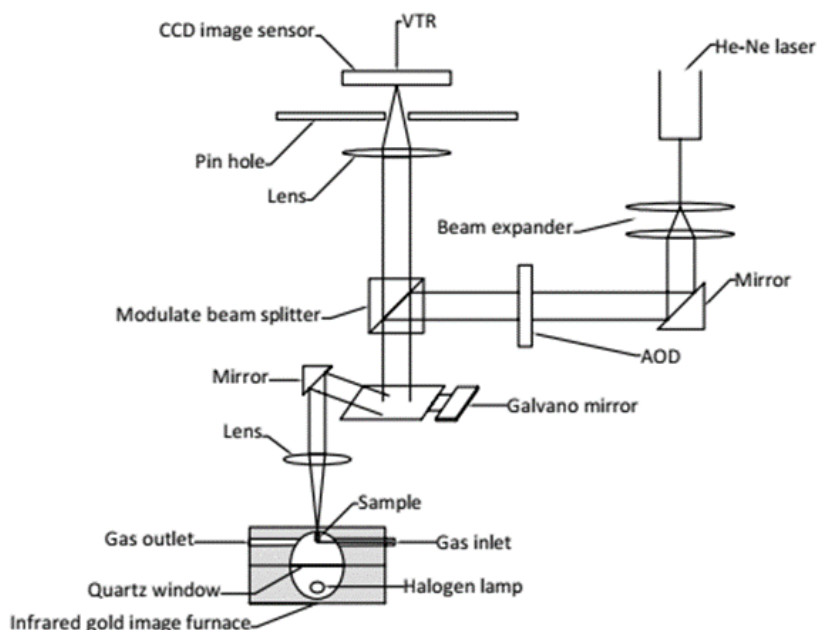
Figure 3.4. Schematic of CSLM [8].

The first step was to calibrate the thermocouple inside the heating chamber. Since the thermocouple lies a few millimeters below the sample separated from it by the alumina crucible, the detected temperature by the thermocouple does not precisely indicate the actual temperature of the sample. Calibration was carried out by melting three samples of pure metals whose melting points are well known. The samples used were copper and nickel. Each sample was placed in the high purity alumina crucible with inner diameter 4.5 mm. The alumina crucible was positioned in the focal point inside the ellipsoid chamber on top of the thermocouple. After sealing it carefully, the chamber was evacuated using a pump connected to the chamber with a hose. Air was evacuated from the chamber until the pressure inside was -98 kPa then it was switched off and pure argon gas was purged into the chamber until it was completely full. To obtain argon with such high purity, argon passes through a Mg furnace heated up at 500 °C prior to entering the heating chamber. Mg reacts with any remnant oxygen mixed with argon. Argon is not introduced into the chamber unless the temperature in the Mg furnace is at least 400 °C. The chamber was then evacuated again. The cycle of argon purging, and evacuation was repeated three times to ensure the thorough cleanliness of the chamber and to get rid of the oxygen remnants inside as much as possible. Oxygen partial pressure was measured using a PO_2 sensor at the gas exit. The partial pressure of oxygen inside the chamber after cleaning by argon was around 1×10^{-18} ppm. The surface of the metal sample was observed using the confocal laser scanning microscope. A few moments after the sample melted, the heating power was reduced progressively until the sample solidified again. The displayed temperature at the moment of solidification was recorded. The same procedure was applied to the three metals. It is worth noting that the displayed temperature by the thermocouple at the moment of fusion is misleading as it includes the heat of fusion in addition to the real melting point, thus, reflecting a higher temperature than the real melting point. Therefore, the recorded temperature at the solidification

point is more accurate. The thermocouple melting points were then compared to the theoretical melting points of the metal samples and the temperature differences were plotted against the given melting points. A straight line connecting the three points was drawn using linear regression. The straight line was used to predict the temperature difference adjacent to the given melting point in the case of our steel samples. Thus, correcting the error value given by the thermocouple. The indicated temperature by the thermocouple was 1600 °C. By interpolation, the real temperature of in-situ observation was determined to be 1541 °C.
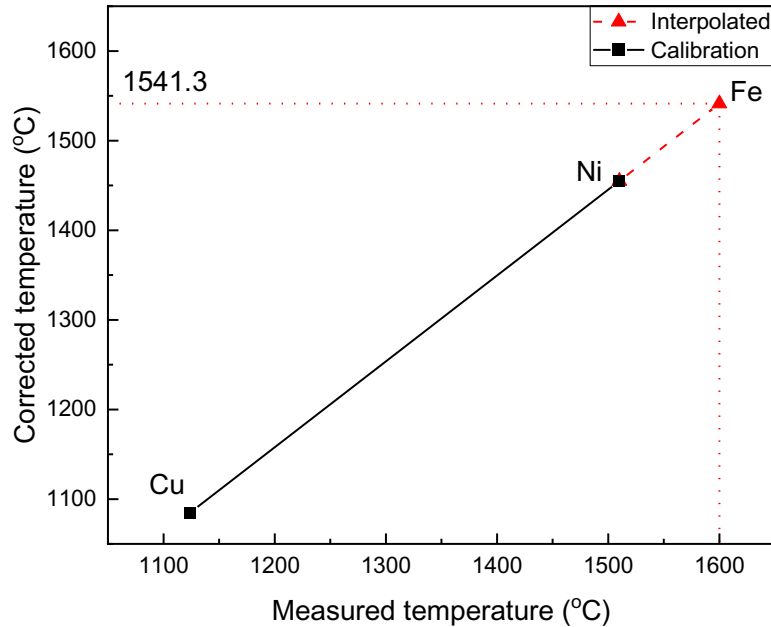
Figure 3.5. Interpolation of the sample temperature based on the corrected values of materials of well-known melting points.

The steel rod produced by GERO furnace was cut into small disks with dimensions of around 4 mm diameter and from 4 to 8 mm height using an abrasive cutting machine. A disk was then placed into the same type of alumina crucible as described in the calibration step. The heating profile was set to 300 °C with a heating rate of 50 °C/min, then it was set on hold for one minute before proceeding to 1500 °C with a heating rate of 200 °C/min. After reaching 1500 °C, it is advisable to use a slower heating rate, so from 1400 °C to 1541 °C the heating rate was 20 °C/min. At 1541 °C, the lens was adjusted to focus on the surface of liquid steel, and the microscope recorded the behavior of inclusions at the surface at a rate of 30 fps. An observation time of one hour was given to detect the inclusions and capture their motion and their moments of coagulation. The details of the temperature profile are given in Figure 3.6..
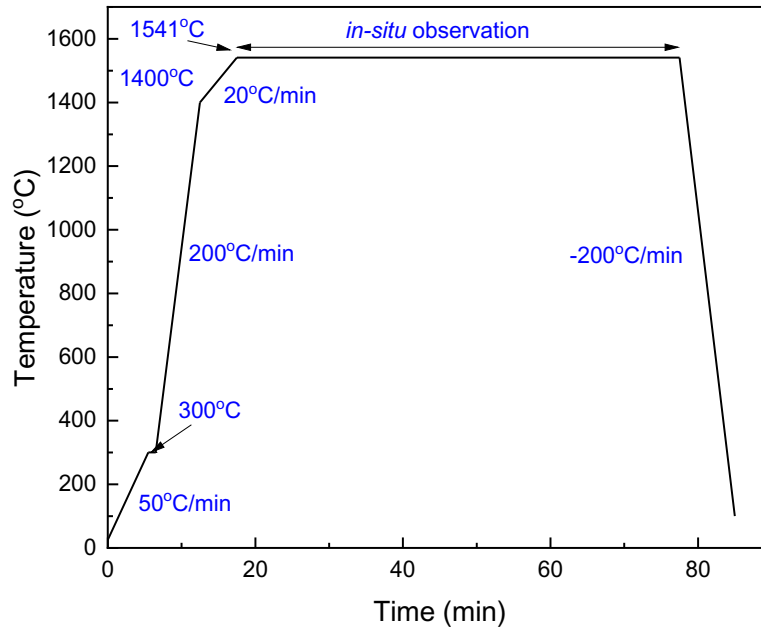
Figure 3.6. Temperature profile of the heating chamber containing the steel sample used in the CSLM *in-situ* observation.

When the sample melts, its surface takes a convex shape indicating that it is hydrophobic with respect to the alumina crucible. Figure 3.7. shows the setup of the sample inside the alumina crucible before and after *in-situ* observation.
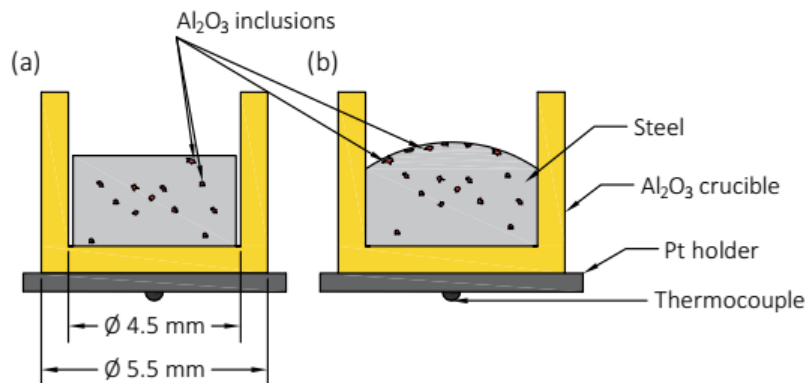
Figure 3.7. Experimental setup: (a) steel sample inside the alumina crucible before CSLM observation. (b) solidified steel sample after CSLM observation preserving the convex surface from the melting stage.

Chapter four: Results and Discussion

In this chapter the results of the chemical extraction and *in-situ* CSLM observation are presented. The SEM images of the chemically extracted inclusions indicate the morphology of alumina inclusions. They refer to the degree of irregularity which is a factor that influences the shape of the contact line around the particle. Additionally, SEM-EDS chemical analysis shows the chemical composition of some typical inclusions. This information is used to estimate the source of undulation in the 3-phase contact line. The CSLM images are analyzed to determine the sizes, velocities, and accelerations of the inclusions. The calculated values are used to determine the attraction force between inclusions. In addition, the drag and inertial forces are calculated. The attraction force is then analyzed using a MATLAB script to determine the type of capillary interaction for each case. Finally, the obtained results are discussed.

4.1. CSLM *in-situ* observation

Once the sample melted, a strong liquid flow was detected. Therefore, a few minutes were given for the sample surface to stabilize before starting the observation as the inclusions were moving so fast that it was very difficult to detect the interaction between them. When the surface flow settled down, the observer began to track the alumina inclusions and their interactions. It is worth noting that the inclusions observed had mostly irregular shapes. Clustering of inclusions started to occur whenever one of them was in the capillary range of the other. Every pair of particles would approach each other at a low speed until the distance between them was in the range of a few micrometers. The particles would then accelerate and agglomerate within less than a second (see Figure 4.1.). In most cases, it was detected that one of the particles or both would rotate around a vertical axis just before agglomeration, as shown in Figure 4.2.. This phenomenon suggests that the meniscus deformation around the particles is in an undulated manner. Therefore, when the orientations of the capillary multipoles were mismatched, one of the particles or both would tend to adjust their orientation to achieve a minimum energy state by rotating around a vertical axis going through their mass centers. This is illustrated in equation (4.1) where the cosine needs to be one to obtain minimum ΔW. This adjustment of the orientation of one particle with respect to the other was accompanied by a high translational acceleration of the smaller particle, subsequently, their agglomeration.

$$\Delta W = -G_o \pi \sigma H_A H_B \cos\left(n_A \varphi_A - n_B \varphi_B\right) \frac{r_A^{n_A} r_B^{n_B}}{L^{(n_A + n_B)}} \tag{4.1}$$

The irregular shapes of inclusions and their sharp tips help penetrate the liquid steel film between them when they approach each other. Once the two particles touch each other, they agglomerate

immediately as the drainage of liquid film from the gap of the particles occurs spontaneously since the inclusions are non-wetting to liquid steel [86].
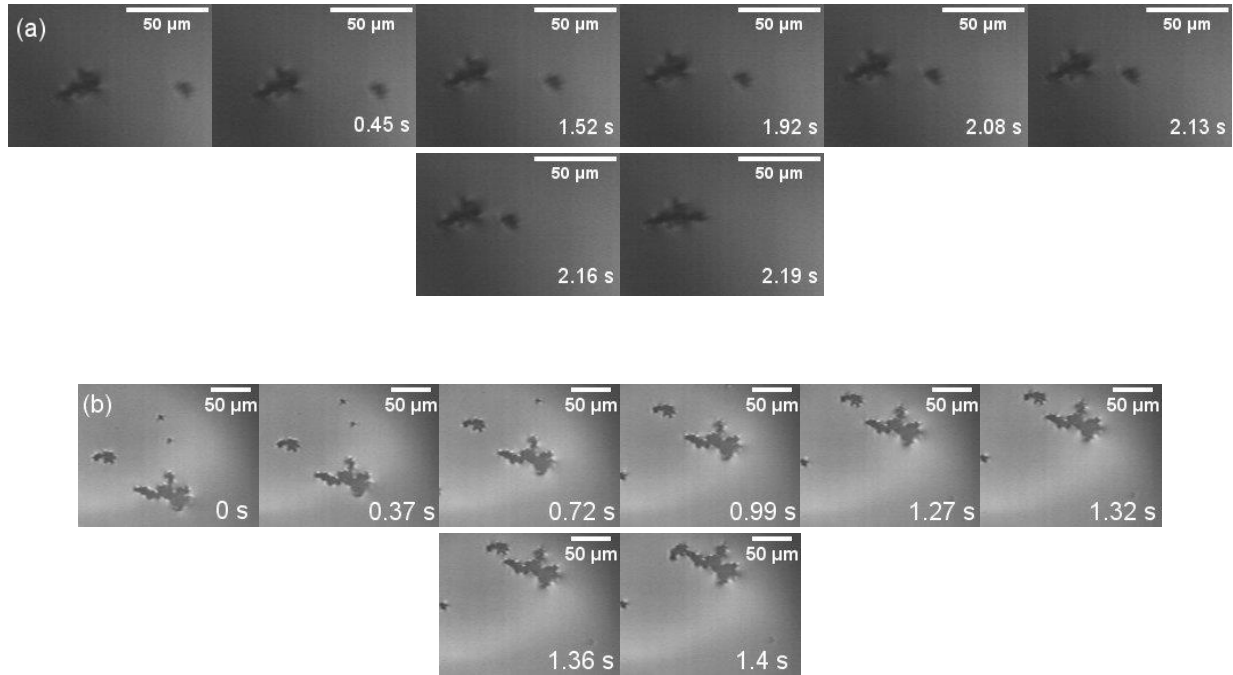

Figure 4.1. Image sequence of the clustering of alumina inclusions at the interface of liquid steel and argon gas at 1541 °C. Sequence (a) is the clustering in case 1 while sequence (b) is the clustering in case 7.
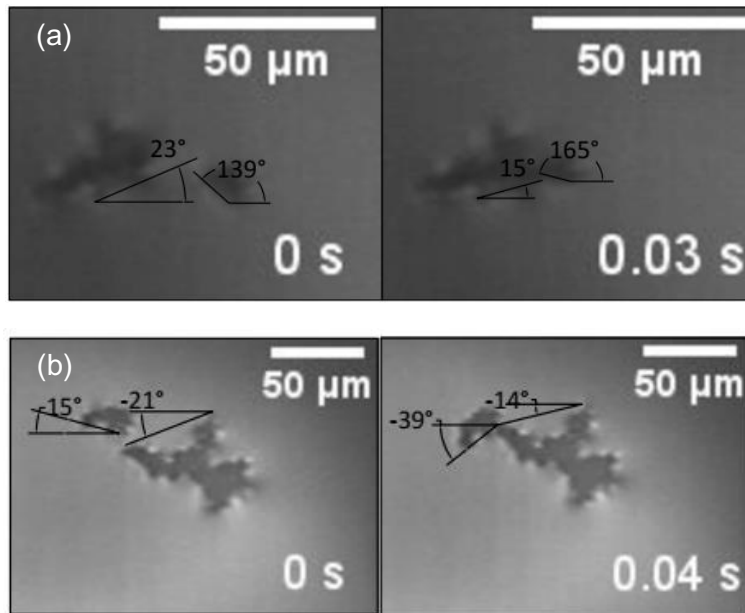

Figure 4.2. Rotation of alumina inclusions around a vertical axis perpendicular to the liquid surface to adjust their orientations before clustering. (a) case 1. (b) case 7.

4.2. The actual acting length versus the theoretical capillary length

The capillary length $q^{-1}\left(=[\Delta\rho g/\sigma]^{-1/2}\right)$ was defined by Paunov et al. [7] as the range within which the capillary interaction arises between two floating particles. The capillary length for the liquid steel/ argon gas system is calculated to be 5.3 mm. However, the actual acting length, ranged from 39.8 to 98.3 µm for all the cases, was much smaller than the theoretical one. Across the 13 cases, the capillary length was 54 to 133 times larger than the actual acting length. The acting length generally increases linearly with the critical radius, as shown in Figure 4.3. The critical radius is given as $\sqrt{R_A.R_B}$ and it used as an indicator for the collective size of the two particles. Larger particles generate greater meniscus deformation with larger domain leading to a larger acting length and a greater attraction force. It is important to note that the certainty of the measured acting length is not very high since the movement of the particles is always influenced by the flow of liquid steel. Additionally, some inclusions arise to the surface at a position very close to another inclusion such that it might be within the acting length of the other inclusion. Finally, the inclusions are often under the influence of more than one capillary force from the surrounding inclusions from different directions, which makes it hard to set apart the effect of one individual case of capillary interaction and the associated acting length.
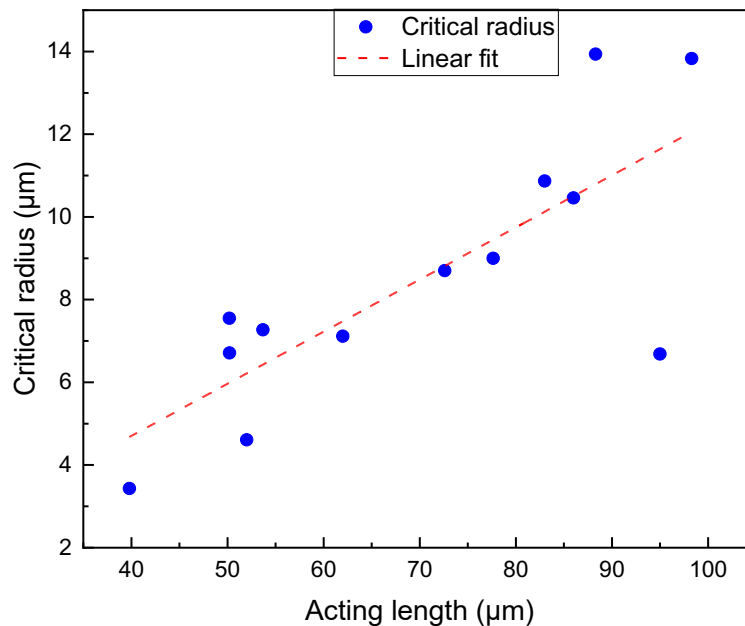
Figure 4.3. The critical radius plotted versus the acting length.

4.3. Shape and chemical composition of inclusions

In this section the results of the SEM-EDS experiments are discussed. SEM analysis was carried out on inclusion samples obtained from chemical extraction to examine the morphology of

inclusions and obtain 3D images of inclusions. EDS was performed on the polished samples before performing the CSLM *in-situ* observation to obtain the chemical composition of some typical inclusions.

Figure 4.4. shows the SEM images of the surface of a polished steel sample typical of the samples used in CSLM observation. The images show that the inclusions have rather irregular shapes. The shape irregularity is one of the potential reasons for the contact line undulation by the pinning of the contact line at some positions on the particle-liquid steel interface, as illustrated by Stamuo et al. [10].

Figure 4.5. shows 3D SEM images obtained from the chemical extraction. Most alumina inclusions have faceted structures which means that they have three-dimensional character and well-developed facet planes. The facet structure results from the slow growth rate of alumina crystals. A slow growth rate allows the crystals to grow with a configuration that minimizes the surface free energy [87]. The sizes of the inclusions range from 3 to 30 μm.
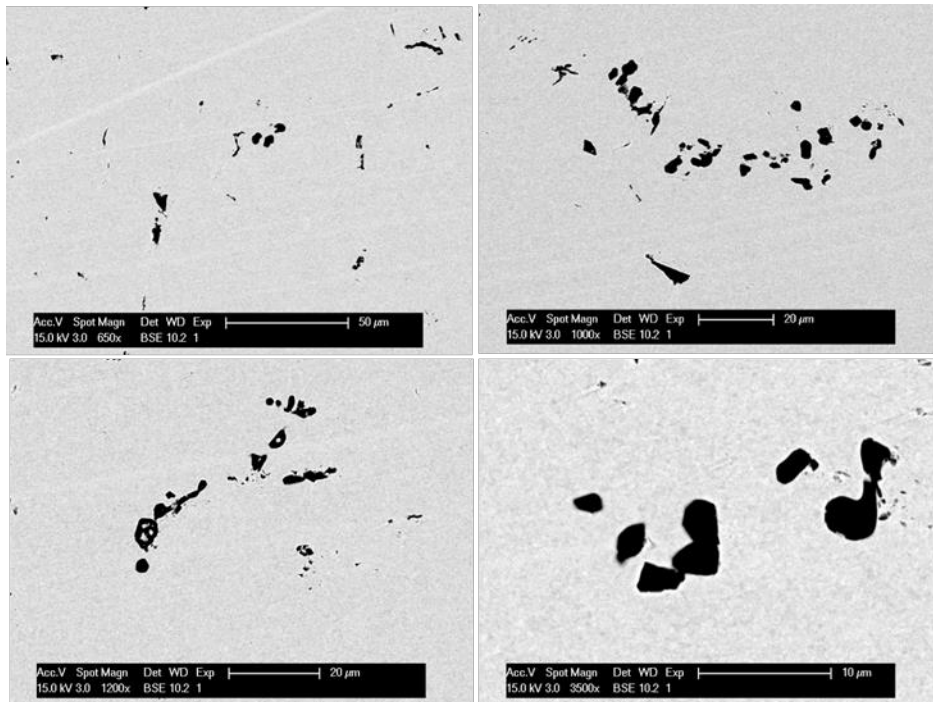
Figure 4.4. SEM images of the surface of a polished steel sample typical of the samples used in CSLM observation. The images show that the inclusions have rather irregular shapes.

Figure 4.6. SEM-EDS chemical analysis of spot 1 from an alumina inclusion obtained from chemical extraction which is typical to the inclusions floating at the liquid steel/argon interface observed by the CSLM.
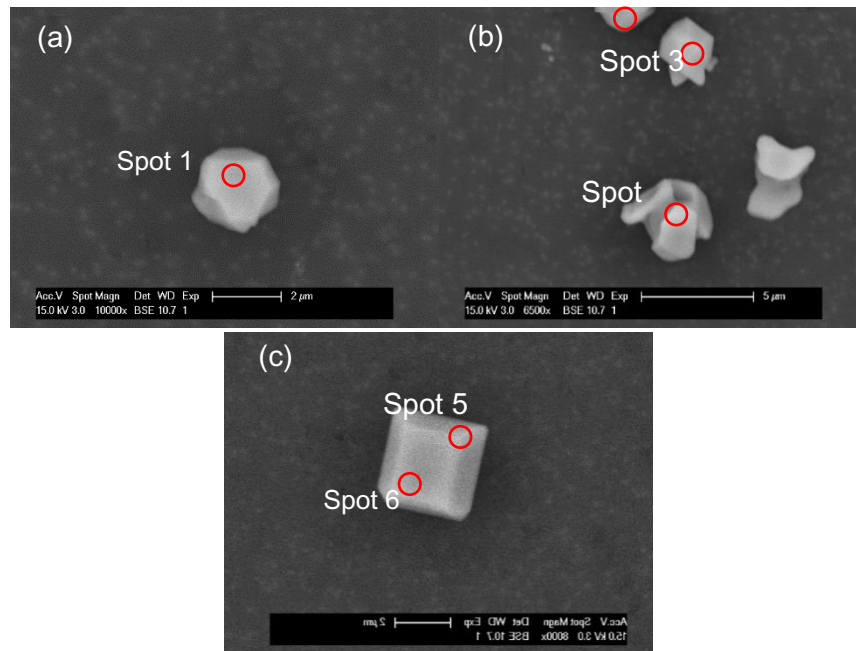
Table 4.1. The chemical composition of typical inclusions examined by SEM/EDS

Spot	Al weight %	O weight %
1	56.51	43.49
2	58.92	41.08
3	53.44	46.56
4	57.88	42.12
5	53.14	46.86
6	60.93	39.07

4.4. Calculation of interaction forces

In this section, the images obtained from in-situ CSLM observation were analyzed to obtain the velocity and acceleration of alumina inclusions at the liquid steel/argon gas interface.

The capillary force on agglomerating particles was calculated using the energy approach introduced by Danov et al. [11] and different multipole orders were examined. Furthermore, the drag resistance force on the particles was calculated according to the equations introduced by Dani et al. [75]. Assuming that the capillary force is equal to the drag force, then the drag force was compared to each of the multipole order models examined using curve fitting and the coefficient of determination R^2 was calculated for each case. The multipole model with the highest value of R^2 with respect to the drag force was considered to be the actual multipole order of that case. Finally, the meniscus profile was simulated based on the calculated undulation amplitude.

To analyze the interaction between alumina inclusions, calculations were carried out on 13 pairs of agglomerating particles which were randomly chosen from the images obtained from the *in-situ* CSLM observation. At first, the calculations of the interparticle distances were done by following the same methods used in the literature [9,88,89]. The images obtained from CSLM *in-situ* observation were analyzed using the commercial software ImageJ. The images were binarized, the background around the particles was subtracted, and by using a proper threshold of darkness level, the inclusions were distinguished from their surroundings. The circularity of the particles was largely disparate and ranged from less than 0.2 to almost 1. The mean circularity was calculated for 27 analyzed particles to be around 0.66. The circularity distribution of some typical particles is shown in Figure 4.7. The degree of circularity is determined using the circularity factor (CF_k) which is given by equation (4.2)

$$CF_k = \frac{4\pi A}{P_k^2}$$

(4.2)

Where P_k is the perimeter of particle k.
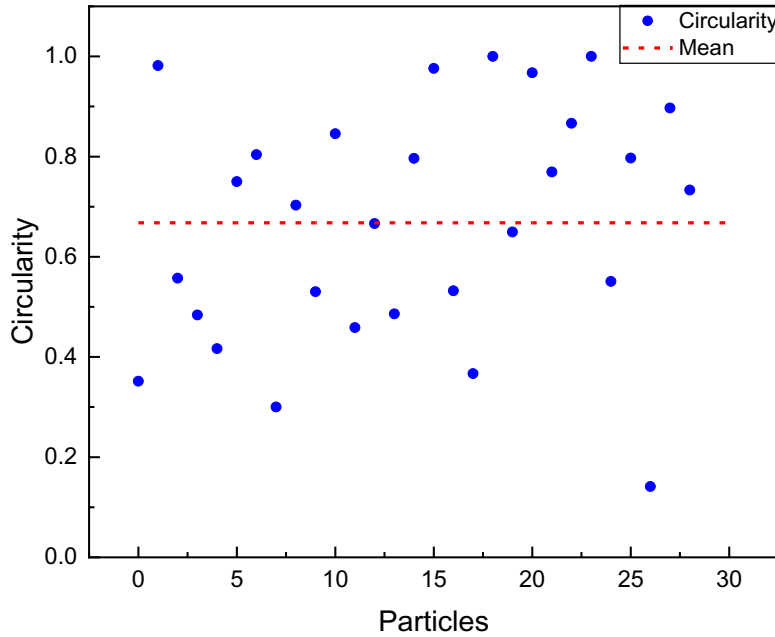
Figure 4.7. Circularity of the projected areas of some of the examined alumina inclusions.

To measure the inter-particle distance, the procedure which was first proposed by Nakajima et al. [89] was applied. It is defined as the distance between the mass centers of the projected 2D particles. This definition implies that the particles are assumed to be discs with uniform thicknesses. This two-dimensional approximation of the irregular three-dimensional inclusions, however, might lead to a degree of uncertainty regarding the experimental values. Moreover, given that the deformation of the meniscus around the inclusions is increased when they approach each other, the contact line position around the particle changes resulting in a change in the position of the particle mass centers. Additionally, the particles might experience rotation while approaching each other, which will change the position of the mass center as well. These factors make the occurrence of inevitable errors during the measurements of the inter-particle distance, which will affect the calculations of velocity and subsequently the acceleration. However, additional procedures were added to the calculations process to mitigate the effect of these factors, as will be explained in the next section. The mass centers of the particles were determined using a code designed for this purpose on MATLAB.

The time interval Δt between each recorded image was set to 0.033 s. The distance between the particles was measured manually for each recorded moment. The acceleration was then calculated using equation (4.3). The calculation method is illustrated in Figure 4.8.

$$a_{Exp} = \frac{2L_2 - L_1 - L_3}{\Delta t^2}$$

(4.3)

Where L_1, L_2, L_3 are the distances between the centers of inclusions at different time moments.
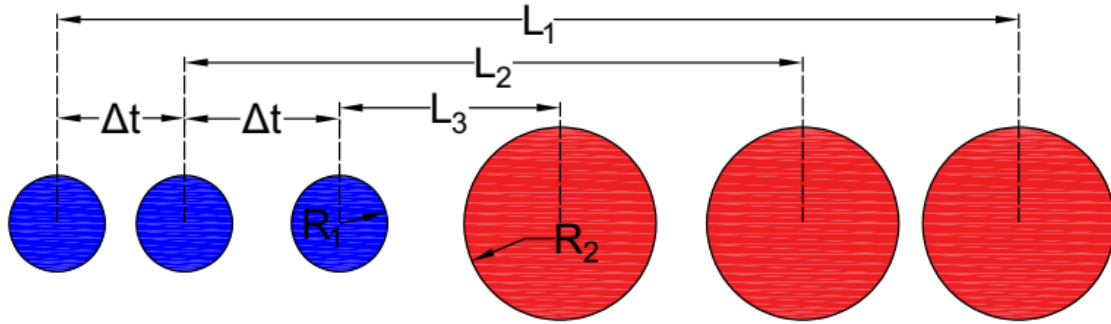
Figure 4.8. Schematic diagram to illustrate the calculation method of the attraction force between the inclusions.

However, this method requires high accuracy of the measured distance. Due to the possible rotation of particles, the change of the immersion depth, and human error evolving from the manual measurement of the inter-center distances, random errors might occur. As a result, the calculated acceleration values were very noisy and did not show any clear trend. Therefore, a fitting curve method was used instead. The recorded distance versus time was smoothed and then fitted into a polynomial equation using a built-in MATLAB function for curve fitting ($L_{(t)} = f(t)$). The order of this polynomial equation was set to 5. The measured distance from CSLM images and the fitted distance are plotted against the elapsed time as shown in Figure 4.9. The total velocity of both inclusions was determined by deducing the first derivative of the polynomial equation obtained from MATLAB (equation (4.4). The acceleration was then calculated using the second derivative of the polynomial function (equation (4.5)). Given that the two particles approached each other, the attraction force was then determined using Newton's second law (equation (4.8)).
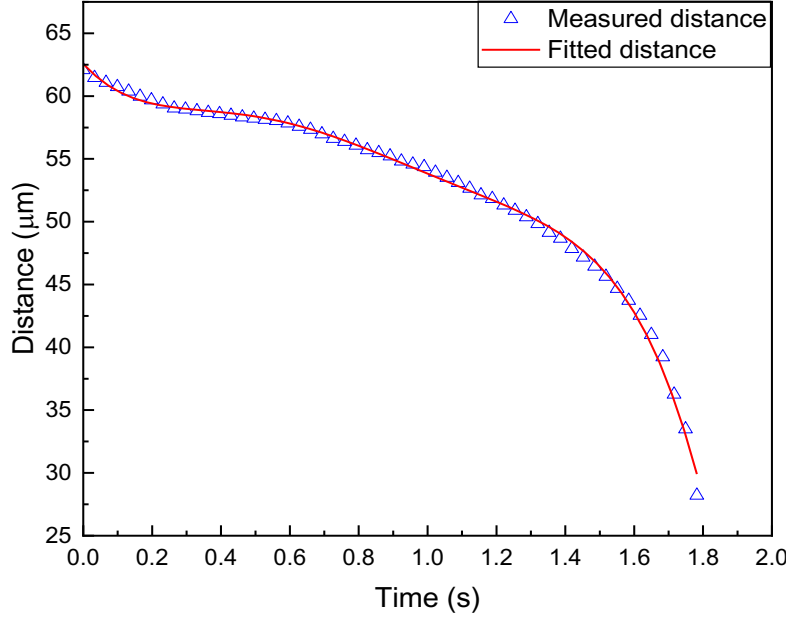
Figure 4.9. Measured and fitted distances between approaching inclusions versus time.

$$v_{tot} = \frac{dL_{(t)}}{dt} = |V_1| + |V_2| \tag{4.4}$$

Where v_{tot} is the total velocity of both inclusions for each moment *i.*

$$a_{tot} = \frac{d^2 L_{(t)}}{dt^2} \tag{4.5}$$

The projected areas of the particles were measured using ImageJ. The area of a given particle was obtained by calculating the average of 5 values measured by the software at different moments. The area was then used to calculate the equivalent radius R_k by equation (4.6).

$$R_k = \sqrt{\frac{A_k}{\pi}} \tag{4.6}$$

The mass of particle *k* was determined by:

$$m_k = \frac{4}{3} \pi R_k^3 \times \rho_{Al_2O_3} \tag{4.7}$$

Where $\rho_{Al_2O_3}$ is the density of alumina, and m_k is the mass of inclusion k.

Then the inertial force was determined as follows:

$$F_{inertial} = \frac{m_A \times m_B}{m_A + m_B} \times a_{tot} \tag{4.8}$$

Where m_A and m_B are the masses of the two inclusions. The parameter $\frac{m_A \times m_B}{m_A + m_B}$ is used when both inclusions are moving.

To determine the type of the capillary force acting on the inclusions, the net force acting on the inclusion (the inertial force) was assumed to be equal to the difference between the capillary force and the drag force. The inertial force, however, was found to be negligibly small compared to the capillary force. When comparing the inertial force to the theoretical capillary force, it was found that the capillary force exceeds the inertial force by 6 to 7 orders of magnitude. The evolution of capillary and inertial forces as two typical particles approach each other is shown in Figure 4.10. Hence, the capillary force was assumed to be equal to the drag force and the inertial force was neglected. In Figure 4.10 it is noted that the curve of the inertial force is taking a sinusoidal shape at large distance. This is caused by the large scattering of the recorded inter-center distance since it is measured manually. Therefore, the fitting polynomial function takes this shape to fit with the noise.
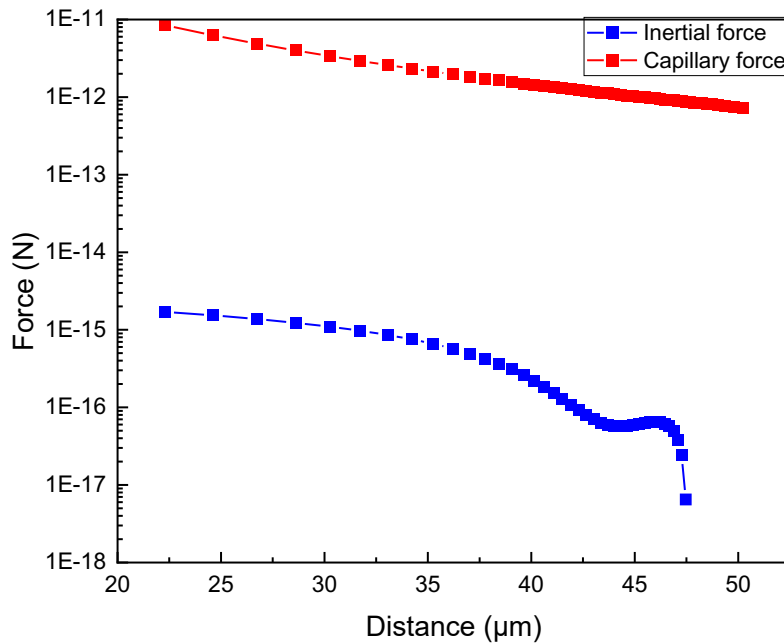
Figure 4.10. Evolution of capillary and inertial forces plotted against the distance between two alumina inclusions. The maximum and minimum plateaus in the end of the inertial force curve are caused by the fitting function attempting to fit the noise arising from the errors which is caused by manual measuring of the inter-center distance.

The drag force is the force opposing the flow of the inclusions and it acts opposite to the direction of the capillary attraction force. Drag force is given by equation (4.9). The magnitude of the drag force is a function of the velocity of the floating particles and their shape. The shape is assumed to be spherical for simplification as stated before. However, only the immersed part of the particle is considered in the drag force calculations because the viscosity of gas is assumed to be zero. The shape contribution in the drag force equation is expressed by the drag coefficient f. f is a function of dimensionless immersion depth b/R_k. b is determined by equation (4.10).

$$F_{drag} = 6\pi\mu R f v G^{-1} \tag{4.9}$$

Where G^{-1} is the mobility function and it accounts for the hydrodynamic resistance that arises when two particles approach each other in a liquid phase.

$$b = R_k(1 + \cos \alpha_k) \tag{4.10}$$

f is then determined by using the least square method with a polynomial function of the fifth order, and it is given by equation (4.11).

$$f = 0.043(^b/_{R_k})^5 - 0.29(^b/_{R_k})^4 + 0.76(^b/_{R_k})^3 - 1.01(^b/_{R_k})^2 + 0.96(^b/_{R_k}) + 0.036 \tag{4.11}$$

Where the ratio $^b/_{R_k}$ is the same for all particles since they all have the same value for α_k.

The capillary force magnitude depends on the distance between the particles, whereas the drag force is proportional to the velocity of the particles. Accordingly, to determine the drag force, the velocity of each particle had to be calculated. Knowing that the drag force is the same for both particles 1 and 2, equation (4.12) is assumed. This equation contains two unknowns V_1 and V_2. Therefore, with the total velocity already determined, equation (4.4) is substituted in equation (4.12) to determine each of V_1 and V_2. With both V_1 and V_2 obtained, the drag force can be calculated.

$$6\pi\mu R_1 f|V_1|G^{-1} = 6\pi\mu R_2 f|V_2|G^{-1} \tag{4.12}$$

The asymptotic expressions of $\Delta W(L)$ for two capillary multipoles introduced by Danov et al. [11] were explored. The first derivative of equation (4.13) was used to determine the capillary force by using different values of n_A and n_B where n_A and n_B are the orders of multipoles of particle A and B respectively.

$$\Delta W = -G_\circ \pi\sigma H_A H_B \cos\left(n_A\varphi_A - n_B\varphi_B\right) \frac{r_A^{n_A} r_B^{n_B}}{L^{n_A+n_B}} \tag{4.13}$$

φ_A and φ_B characterize the rotation of respective particles around a vertical axis. The parameter $n_A\varphi_A - n_B\varphi_B$ was assumed to be always zero, leading to a constant value of $\cos\left(n_A\varphi_A - n_B\varphi_B\right)$ equal to 1. This is based on the assumption that the particles were always free to rotate around their vertical axes to achieve minimum free energy. Accordingly, the cosine expression was neglected, and the equation used in the MATLAB code for capillary force F_{Cap} was reduced to:

$$F_{Cap} = (n_A + n_B)G_\circ \pi\sigma H_A H_B \frac{r_A^{n_A} r_B^{n_B}}{L^{n_A+n_B-1}} \tag{4.14}$$

The density of pure liquid steel at the observation temperature used in the calculations is 6980 g/cm³. It was obtained using equation (4.15) introduced by Jimbo et al. [90] which is a function of temperature and carbon content produced by a least-square analysis of their experimental data points. The theoretical density of pure alumina was taken as 3.95 g/cm³.

$$\rho[g/cm^3] = (7.1 - 0.0732 \times \%C) - (8.28 - 0.874 \times \%C) \times 10^{-4}(T - 1823) \tag{4.15}$$

The surface tension σ for pure iron at around 1814 K is 1.918 N/m. It is estimated using equation (4.16) which was obtained from least-square analysis of surface tension values obtained from experiments done by Kasam et al. [91].

$$\sigma[N/m] = 1.918 - 0.00043(T - 1811) \tag{4.16}$$

The contact line radius for particle k is given by equation (4.17).

$$r = R_k \sin(\alpha_k) \tag{4.17}$$

Where α_k is the contact angle between pure alumina inclusions and liquid steel which is equal to 137° [92].

The amplitude of contact angle deformation H_k is given by:

$$H_k = {}^1\!/_2 \, R_k \Delta\alpha_k \sin(\alpha_k) \tag{4.18}$$

Whereas R_k and α_k for a given particle are known from the CSLM image and the particle composition respectively, the CAH ($\Delta\alpha_k$) remains the only unknown variable in this equation. The hysteresis of the contact angle depends on the particle shape and the pining of contact line at the edges of the particle. Although the undulation of the contact line can be observed from the CSLM images, $\Delta\alpha_k$ cannot be measured from those images directly. Therefore, $\Delta\alpha_k$ is first deduced using an iteration process in which different values of $\Delta\alpha_k$ are inserted in equation (4.18) to determine the value of H_k that will give the most fitting capillary force relative to the drag force. The latter is derived from the minimum sum of squared residuals (SSR) of the difference between the capillary force and the drag force. The range of angle hysteresis values is between 0° and 10° and the step was 0.01°. it is found that when increasing the value of $\Delta\alpha_k$ the SSR value decreases first until it reaches a minimum and then it increases monotonically. The value of $\Delta\alpha_k$ that corresponds to the minimum SSR is considered in the calculations of the capillary force F_{Cap}.

As all the inputs required for solving equation (4.14) are obtained, the capillary force is determined using different values of n_A and n_B.

4.5. Type of capillary interaction

To determine which type of capillary interaction applies in each case of inclusion collisions, capillary forces at different multipole orders were compared to the calculated drag force and the inertial force. The capillary interaction force as a function of distance was then compared to the drag force. The degree of agreement between the two forces was determined by calculating the coefficient of determination (R^2) for each case. R^2 is given by equation (4.19). Multipole models starting from $n = 1$ up to $n = 4$ were used in the calculations. The multipole model which gives the greatest value of R^2 was considered the best model to describe the capillary interaction for the given case.

$$R^2 = 1 - \frac{S_{res}}{S_{tot}} \tag{4.19}$$

Where S_{res} is the sum of squared regression of the difference between capillary force and drag force $S_{res} = \sum(F_{Cap} - F_{drag})^2$. And S_{tot} is the total sum of squares of the difference between the

drag force and the mean drag force values ($\hat{F}_{drag}$). $S_{tot} = \sum(F_{drag} - \hat{F}_{drag})^2$. The values of R^2 for the analyzed cases are shown in Table 4.2. Figure 4.11. shows the drag and the best fitted capillary forces from the multipole models for cases 1-4. The first three cases exhibit the DP-QP interaction whereas the fourth case exhibit the DP-DP interaction.
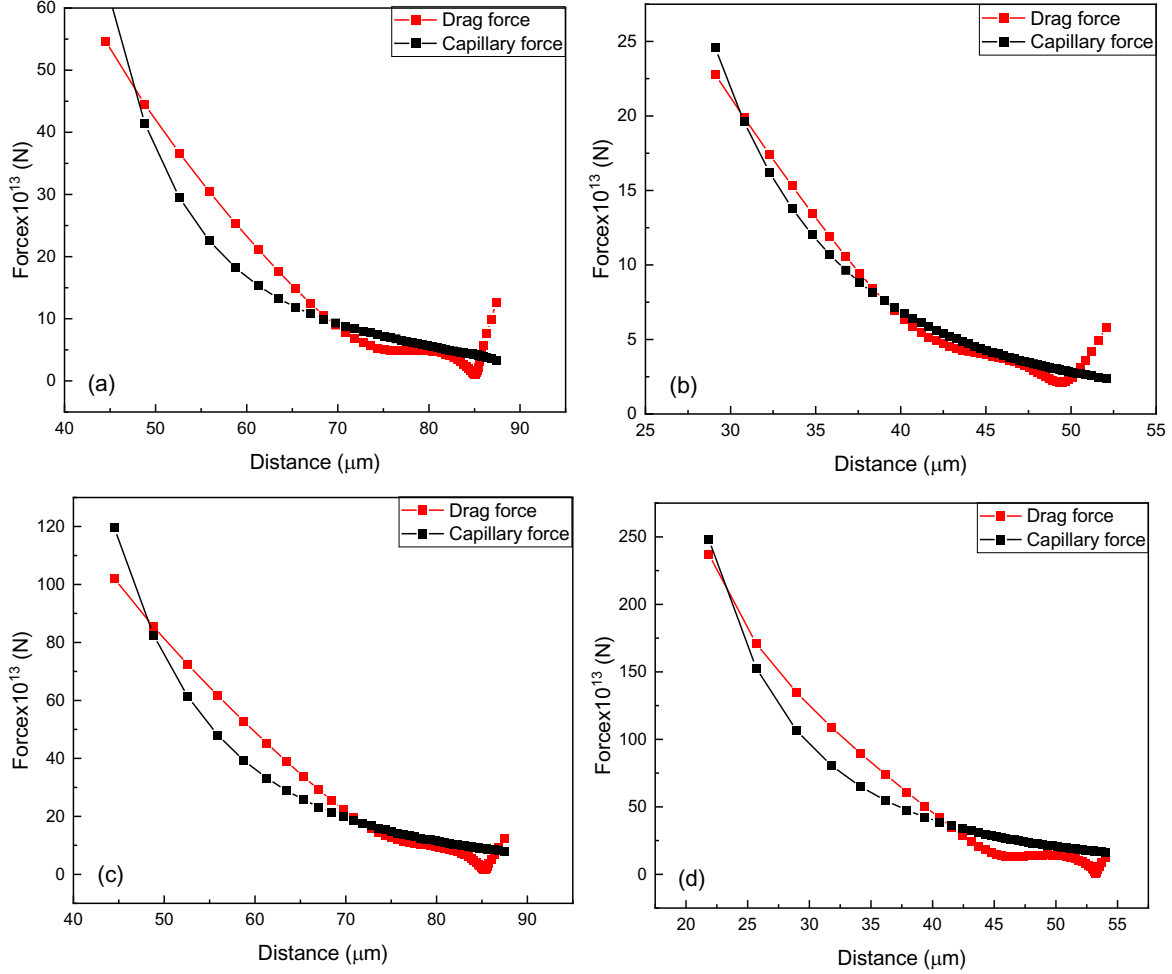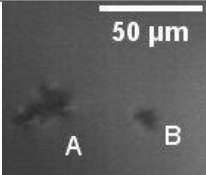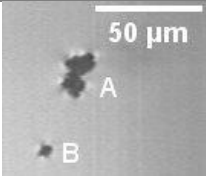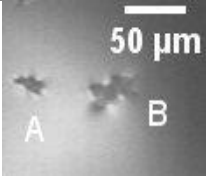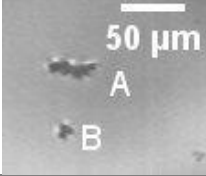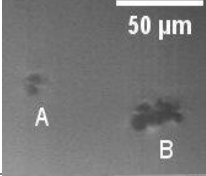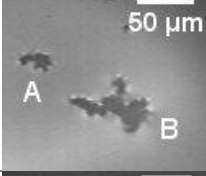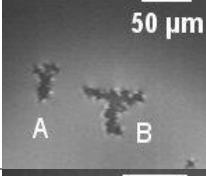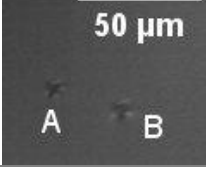
Figure 4.11. Drag and capillary forces calculated using the CSLM image sequences and the capillary multipole model. (a) Case 1, (b) Case 2, (c) Case 3, and (d) Case 4.

Table 4.2. R^2 values for the analyzed cases and their orders of multipoles based on the calculations.

Case	Picture	Areas (1, 2) [µm]	R²					Order of multipole (A, B)
			DP-DP	DP-QP	QP-QP	QP-HP	HP-HP	
1		298.15, 84.79	0.8414	0.9027	0.8211	0.6858	0.5509	(2,1)

2		189.53, 23.47	0.8793	0.9595	0.9030	0.7598	0.5818	(2,1)
3		193.88, 608.77	0.8520	0.9254	0.8571	0.7279	0.5922	(2,1)
4		298.04, 87.17	0.9197	0.8819	0.7536	0.6288	0.5285	(1,1)
5		62.65, 313.86	0.8607	0.9234	0.8375	0.6886	0.5355	(2,1)
6		231.38, 138.44	0.7550	0.8911	0.9354	0.8966	0.7976	(2,2)
7		263.68, 1409.9	0.5845	0.7651	0.8861	0.9345	0.9196	(2,3)
8		397.4, 907.26	0.8359	0.9364	0.8939	0.7817	0.6557	(2,1)
9		350, 161.4	0.8180	0.9453	0.9465	0.8580	0.7270	(2,2)
10		27.21, 50.13	0.8332	0.8890	0.8011	0.6511	0.4962	(2,1)
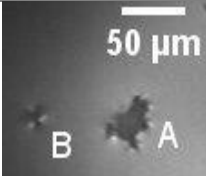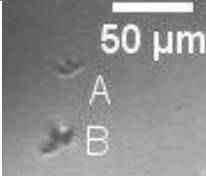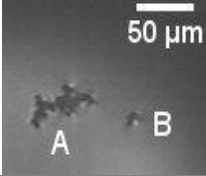
11		839.2, 163.99	0.8292	0.9310	0.9058	0.7999	0.6613	(2,1)
12		105, 190.15	0.9440	0.8992	0.7392	0.5645	0.4124	(1,1)
13		685.4, 94.53	0.6309	0.804	0.9048	0.9265	0.885	(2,3)

Table 4.3. Angle hysteresis for different cases at different multipole orders.

Case	Order of multipole	Angle hysteresis
1	(2,1)	0.79, 0.15
2	(2,1)	0.71, 0.62
3	(2,1)	0.51, 0.17
4	(1,1)	1.46, 0.04
5	(2,1)	0.93, 0.42
6	(2,2)	2.08, 0.05
7	(2,3)	3.39, 0.07
8	(2,1)	0.41, 0.13
9	(2,2)	2.33, 0.07
10	(2,1)	0.82, 0.17
11	(2,1)	0.52, 0.47
12	(1,1)	0.97, 0.03
13	(2,3)	5.92, 0.36

Out of 13 cases of capillary interactions examined, 7 cases followed the DP-QP model, two cases were DP-DP, two cases were QP-HP, and two cases followed the QP-QP model. The DP model is considered to be forbidden since it would generate a moment that would act on the particle and cause it to rotate continuously around a horizontal axis (See Figure 4.12.). the rotation can be

stopped under the effect of barriers in the fluid. However, in our case the particles were assumed to be free to move but no rotation along a horizontal axis was recorded. Because the inclusion particles were not perfect spheres, rotation under the effect of DP moment did not occur. To justify the DP model, the alumina inclusions were assumed to be more like disks rather than spheres in the real situation. Nevertheless, the mathematical models derived by Danov et al. [11] treat the floating particles as spheres. The derivation of a modified theoretical model for disk-shaped floating particles is thus required to reduce the error and achieve a more accurate evaluation of the capillary interactions between the alumina inclusions.

Table 4.3 shows the angle hysteresis of both particles for each case. It is clear that the magnitude of angle hysteresis increases with the order of multipole. In the case of QP-HP model, the angle hysteresis of one particle is 3.39° and 0.07° for the other. In the case of DP-DP model, the angle hysteresis are 1.46° and 0.04°. Most of the cases show small angle hysteresis. Moreover, it is noticed that the angle hysteresis increases with increasing the order of multipole. Though not in a consistent manner. The smallest value of angle hysteresis occurs in case 12 which follows the DP-DP model. Whereas the largest two recorded angle hysteresis occur at cases 7 and 13 (3.39 and 5.92) which follow the QP-HP model.
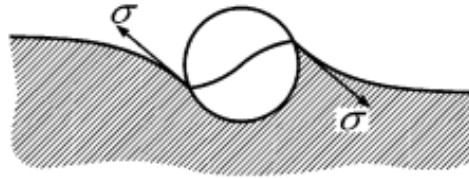
Figure 4.12. A schematic diagram of a floating particle subjected to capillary DP moment which forces the particle to rotate continuously to annihilate this moment.

For the capillary attraction force to be effective, the capillary interaction energy needs to exceed the thermal energy KT, where K is boltzmann constant. The thermal energy causes the inclusions to move in a random manner. The ratio of the capillary interaction energy to the thermal energy is around 100 in the case of QP-QP and it is up to 10000 in the case of DP-DP. The ratios of capillary interaction energy to thermal energy for DP-DP, DP-QP, and QP-QP models plotted against the inter-center distances between particles are shown in Figure 4.13. The figure also shows that the interaction energy is dropping with raising the order of multipole. this is because a higher multipole order gives larger attraction force as shown in equation (4.14), and larger attraction force is associated with smaller interaction energy (equation (4.13)).
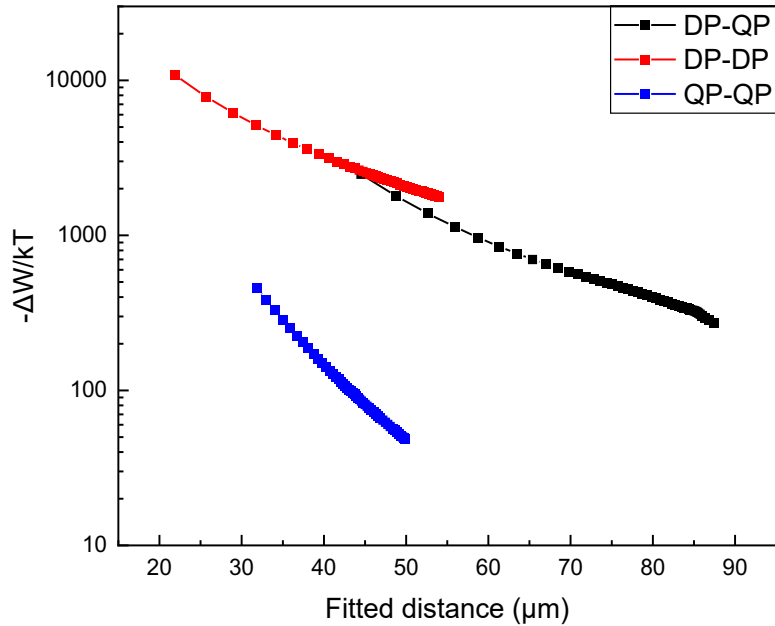
Figure 4.13. The ratio of capillary interaction energy ($-\Delta W/kT$) plotted in a semi-log scale against the fitted inter-center distance between the approaching inclusion particles. Cases 1, 4, and 6 are shown which exhibit DP-QP, DP-DP, and QP-QP models respectively.
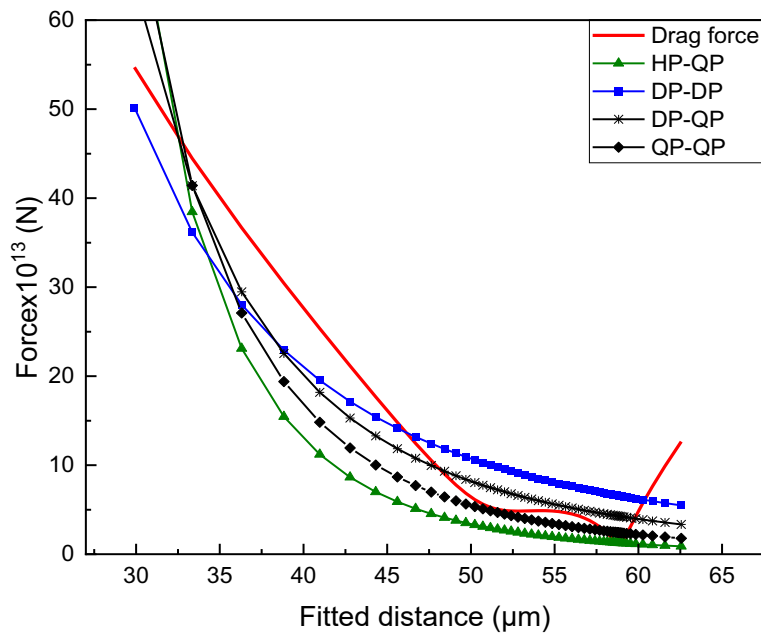
Figure 4.14. Capillary forces extracted from different capillary interaction models and drag force plotted against the distance between two approaching alumina inclusions for case 1. In this case the DP-QP type is the most fitting with respect to the drag force since the curve of the drag force and the curve of the DP-QP force give the highest value of R^2.

It was found that the capillary force derived from the multipole model counterbalanced the drag force. The attraction force increases greatly with the decrease in the interparticle distance. Which

corresponds to the power law relationship between the capillary force and the separation distance between the inclusions in equation (4.14). Different orders of multipoles showed small differences in the calculated attraction forces. At a smaller order of multipole, the initial attraction force at the beginning of the interaction between the two inclusions is slightly larger than the initial attraction force with increasing the order of multipole (see Figure 4.14). As the distance between the inclusions decreases, the slope of the attraction force versus the interparticle distance rises with the order of the multipole. For case 1, the different orders of multipole are plotted together against the fitted interparticle distance in Figure 4.14. Moreover, at a large interparticle distance, a large deviation between the calculated drag force and the capillary force derived from the multipole model is always observed. As the capillary force always increases with higher rate than the drag force as the particles come close. This deviation may be due to the simple assumptions in the capillary multipole model, including the assumption of a spherical shaped particles. Besides, the capillary multipole model assumes a symmetric shape of the undulated contact line, while in reality, the contact line might have a more complex contact line shape depending on the roughness of the particle and its irregular morphology.

In addition to the multipole model used for the undulated contact line, the capillary force was also calculated using the charge model used for a uniform contact line, and the attraction force extracted from both models was compared. In order to do that in the second case -where the best fitting model is the DP-QP model- one particle was assumed to have a QP-shaped contact line while the other DP particle was replaced with a charge. It was found that the DP-QP attraction force was much larger than the charge-QP attraction force by around three orders of magnitude. The attraction force from the charge model clearly would not counterbalance the drag force unlike the multipole model attraction force. The comparison between the forces from the charge and the multipole models is illustrated in Figure 4.15.
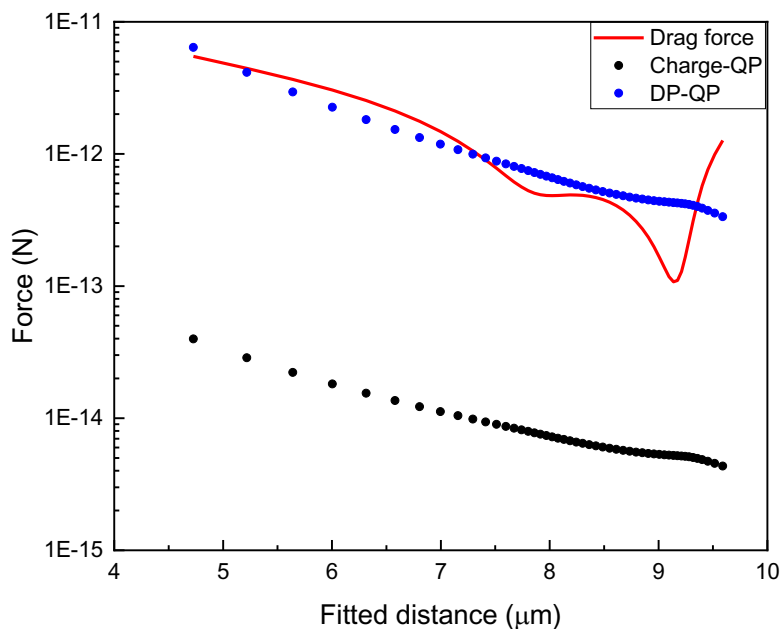
Figure 4.15. Capillary interaction force calculated for the same case using the charge model (in black) and the DP model (in blue). The DP model force is much larger than the charge model force and counterbalances the drag force (red line).

The 13 analyzed cases are summarized in Figure 4.16. The capillary force increases for a given interparticle distance with the collective particles' size expressed by the critical radius. The figure also shows that the minimum distance between particles increases with the critical radius. Only in case 4 the inter-center distance is smaller because the larger particle in this case has an elongated shape and collides with the smaller particle at the longer side so that the inter-center distance is small though the critical radius and hence the capillary force are relatively large.
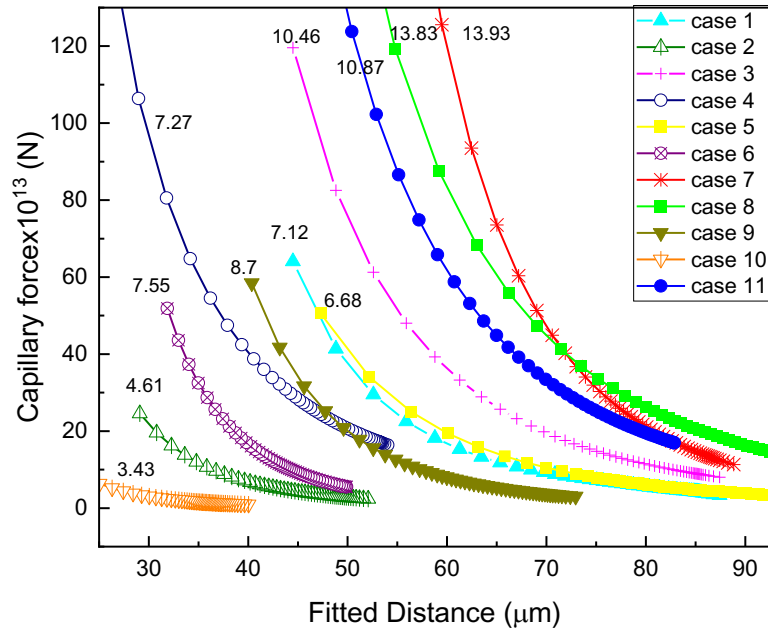
Figure 4.16. Capillary forces for different cases with the critical radius of each case on top of the curve.

4.6. Comparison between the equivalent radius and the effective radius

In a previous study done by Mu et al. [9] they compared the calculations derived using the equivalent radii of inclusions to those derived using the effective radii. In their study, the charge Paunov model was considered [7], which assumes uniform contact line around the floating inclusion. In their calculations they did not consider the drag force acting against the anti-direction of particle movement. Instead, they only considered the inertial force and assumed it to be equal to the capillary attraction force. They used both the equivalent and the effective radii on the same case to determine which one gives better matching with the theoretical model. It was concluded that the effective radius is more suitable for small particles (<20 µm) or for particles that have a large circularity factor (around 0.8). Whereas the equivalent radius is more suitable for larger size particles or with low circularity factor. The effective radius is given by equation (4.20) which is a

scaled-up equivalent radius by its circularity factor. It is worth noting that according to the model they applied, the particle size is the main parameter defining the capillary attraction force. In our case, the amplitude of undulation is however, the main parameter and not the particle size [11].

$$R_{k,eff} = R_k \Big/ \sqrt{CF_k} \qquad (4.20)$$

In general, the calculations based on $R_{k,eff}$ show a slightly higher matching between the capillary and the drag forces expressed in a larger value of R^2 relative to the equivalent radius-based calculations. Nevertheless, in some cases $R_{k,eff}$ results in different order of multipole. The comparison between calculations based on the equivalent and the effective radii is illustrated in Table 4.4. In case 7, the equivalent radius of the larger particle is greater than 20 µm and the circularity factor is 0.257. Thus, the equivalent radius was used for the larger particle while the effective radius was used for the smaller particle. The resulted R^2 is slightly larger than that obtained using the equivalent radius for both particles. The drawback of using the effective radius is that it assumes a much larger radius value. As a result, to measure the attraction force the maximum distance between the approaching particles must be reduced and therefore, the distance(s) measured just before collision must be neglected since the distance between the particles cannot be smaller than the sum of radii of the two particles. This step in the calculations reduces the reliability of the effective radius method since the distances measured at the moments just before the collision are vital for calculating the acceleration and thus the attraction force. Hence, it is concluded that the equivalent radius remains more reliable in the calculations given that the difference in R^2 is not significant but the equivalent radius method allows for including more distances measured before collision for more reliable measurements.

Table 4.4. Comparison between R^2 values derived using the equivalent and the effective radii.

Case	Order of multipole derived from R_k	R^2 based on R_k	Order of multipole derived from $R_{k,eff}$	R^2 based on $R_{k,eff}$
1	(2,1)	0.9027	(2,1)	0.9132
2	(2,1)	0.9595	(2,1)	0.9609
3	(2,1)	0.9254	(2,1)	0.9485
4	(1,1)	0.9197	(2,1)	0.8939
5	(2,1)	0.9234	(2,1)	0.9291
6	(2,2)	0.9354	(2,2)	0.9413
7	(2,3)	0.9345	(2,3)	0.9382
8	(2,1)	0.9364	(2,1)	0.9467
9	(2,2)	0.9465	(2,2)	0.9667
10	(2,1)	0.8890	(2,1)	0.8945
11	(2,1)	0.9310	(2,3)	0.9645
12	(1,1)	0.9440	(1,1)	0.9407
13	(2,3)	0.9265	(3,3)	0.9091

4.7. Meniscus profile

At low temperature-systems, experimental methods were developed to measure the deformation of the meniscus profile. Loudet et al. [70] introduced an experimental method using Phase-shifting interferometry (PSI). In this method, the inclusion floating at water-gas interface is trapped using argon ion laser beam. The radiation pressure forces trap the inclusion in a fixed position. Images of the interface are then captured by a video microscopy. Finally, using the optical phase difference, the height of the meniscus is deduced with high resolution (50 nm). This method, however, cannot be utilized in high-temperature liquid steel systems since the optical laser trapping cannot be applied to a non-transparent medium. Therefore, measuring the meniscus deformation of alumina inclusions at the liquid steel/argon gas interface is not applicable experimentally. Instead, the meniscus shape is reconstructed by the capillary multipole model depending on the calculated capillary force and the size of the given inclusions.

A MATLAB script was utilized to simulate the meniscus shape around each inclusion. The images obtained from the *in-situ* CSLM observation were converted into a mesh where the positions of the mass centers of each particle were identified on XY coordinates. The CAH obtained from calculations (Table 5) and the equivalent radii of the particles were used as inputs in the MATLAB script to generate the shapes of the meniscus around the particles. The particles are assumed to be perfect spheres. Simulated images of the meniscus profiles for typical cases of capillary interactions are shown in Figure 4.17. to Figure 4.20. The images show DP-QP, DP-DP, QP-QP and QP-HP models respectively. The figures show that the meniscus elevation around the particle is reinforced by the meniscus elevation of the approaching particle, causing them to approach each other with an accelerated way. To achieve this position, one or both inclusions rotate around their vertical axes to adjust their orientations and have a constructive superposition.

Figure 4.17. shows the interaction between a DP and a QP inclusions in case 1. It shows how the menisci of these inclusions combine resulting in a superposition of menisci deformations. Before reaching this situation, the inclusion rotates around a vertical axis to orient the meniscus perturbation towards the corresponding perturbation of the other inclusion. The driving force of this behavior is the tendency of the system to minimize the free energy and maximize the attraction force. Figure 4.18. shows the interaction between two dipoles in case 4. The smaller particle has a very small meniscus deformation that is not visible in the figure. Thus, it appears to be completely consumed by the large particle meniscus. Figure 4.19 shows the interaction between two quadrupoles in case 6. In this case the meniscus deformation of the smaller particle is also much smaller than the meniscus deformation of the larger particle. The figure shows the superposition of the convex interfaces of the two particles while the concave part of the interface of the smaller particle disappears as it is dominated by the convex interface of the large particle.
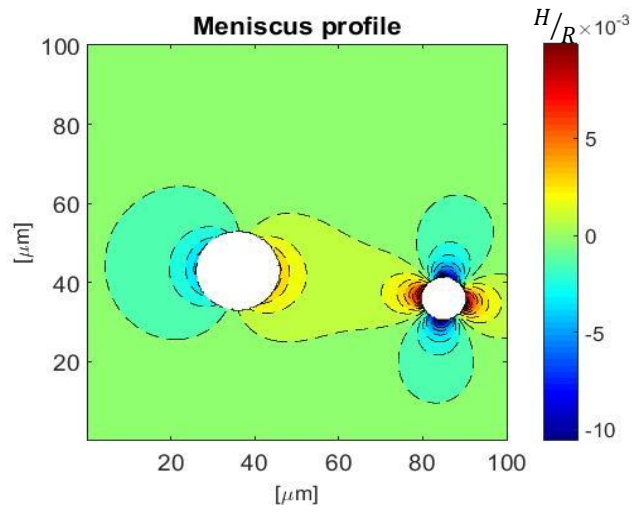
Figure 4.17. Meniscus profile around the two inclusions from case 1 showing a DP-QP capillary interaction.
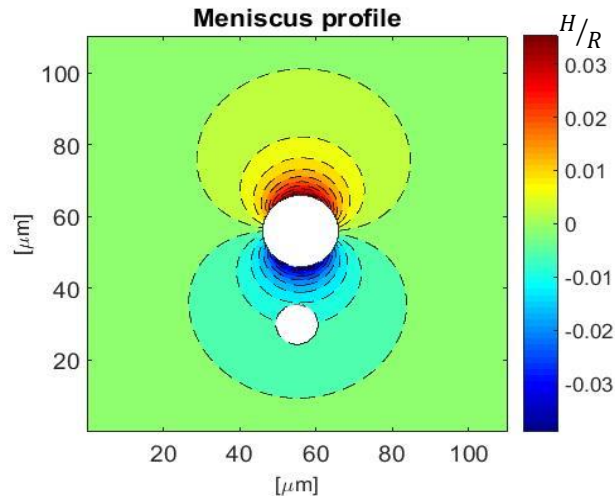
Figure 4.18. Meniscus profile around the two inclusions from case 4 showing a DP-DP capillary interaction.
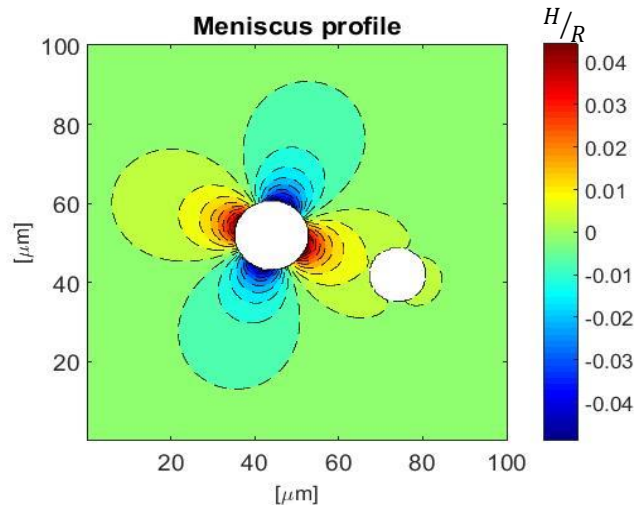
Figure 4.19. Meniscus profile around the two inclusions from case 6 showing a QP-QP capillary interaction.
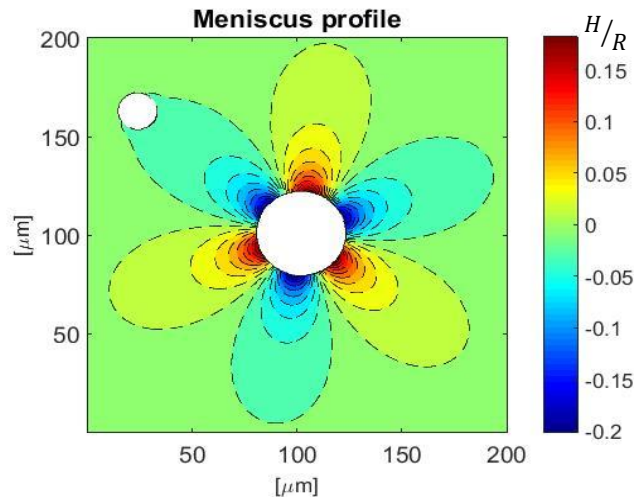
Figure 4.20. Meniscus profile around the two inclusions from case seven showing a HP-QP capillary interaction. The amplitude of undulation at the smaller particle is very small so the range of contact line deformation is short and does not show on the map.

In the capillary multipole model, the meniscus deformation is assumed to be rotationally symmetrical around the particle center. In addition, the particle is assumed to be a perfect sphere. This simplifying assumption doesn't reflect the real situation since the particles are almost never spherical and the surface roughness are not uniformly positioned along the particle surface. Therefore, the results of the capillary multipole models deviate from the calculated drag force. Moreover, the reconstructed meniscus profiles are simplified and doesn't necessarily show the real meniscus shape around the inclusion particles. Hence, the real meniscus shape is expected to be rather complex.

Chapter five: Conclusions

In this master's thesis, the behavior of alumina inclusions on the liquid steel/argon gas interface was investigated. Alumina inclusions are the most common type of inclusions in the clean steel industry since Al is used in this process to clean the steel from oxygen. In addition, alumina can also come from refractories or slags. Alumina inclusions have an important role in influencing the properties of steel as well as affecting the CC process. Inclusions act as crack initiation sites and can be detrimental to the mechanical properties of steel. While large clusters are more likely to float to the surface under the effect of buoyancy and thus, be absorbed by the slag and easily removed from steel. Micro inclusions are more difficult to remove and need a catalytic factor to help remove them. Currently, the most common method to remove inclusions is argon gas injection. Argon bubbles pick up the inclusions and lift them to the surface. This method is effective in removing micro inclusions. The clustering of inclusions on the bubble surface due to the capillary attraction force results in larger inclusions which become easier to pick up by argon bubbles.

The theory of lateral capillary interaction was used to explain the attraction force between floating NMIs at the liquid steel/argon gas interface. However, some simplifications were assumed in the theoretical model, which led to theoretical attraction forces much less than the experimentally recorded forces. One of these assumptions was that the three-phase contact line between the floating particle surface, the gas phase, and the liquid is uniform. Later, this assumption was modified, and a new model was introduced to describe the attraction force in the case of the undulated contact line. This model was able to justify the strong attraction force between micro-inclusions. The last modified model has been used in this thesis and applied to pure alumina inclusions. The model assumes spherical-shaped particles with undulated contact lines. The shapes of undulation are assumed to be symmetrical around the floating particle. In this model, the capillary attraction force is more dependent on the magnitude of contact line undulation than the particle size.

The calculated lateral capillary attraction force for micro alumina inclusions was much larger than the capillary attraction force derived from the charge model. The former could be three orders of magnitude greater than the later one. In the capillary charge model, a uniform contact line was assumed, which was unable to justify the large attraction force between micro inclusions. While the capillary charge model assumes that the capillary attraction force arises mainly from the gravitational force that causes a deformation in the three-phase contact line. At such a small particle size, the capillary force should be diminished, which was not the case with micro alumina inclusions. The capillary multipole model, on the other hand, assumes an undulated contact line due to its pinning at some positions on the particle surface, which induces large interaction energy. This strong capillary interaction can justify the observed strong attraction force between micro alumina inclusions.

In addition, the attraction force derived from the capillary multipole model counterbalances the drag force resisting the particle motion. This suggests that the conventional charge model does not apply to these inclusions and that the meniscus shape around the alumina particles is undulated. The undulation of the contact line is attributed to the heterogeneous chemical composition, irregular shapes, and/or rough surfaces. In this case, as the SEM-EDS chemical analysis showed that the inclusions were pure alumina. Therefore, unless there was an undetected small concentration of surface-active elements at the surface of alumina inclusions, the source of contact line undulation could only be the surface roughness and the shape irregularity. The examination of chemically extracted inclusions showed that most inclusions had irregular shapes (small circularity factor), whereas a few of them had faceted structures. While the surface roughness was not examined, both of the shape irregularity and the surface roughness contribute to the undulating meniscus deformation .

Alumina inclusions start to attract each other at an acting length less than the theoretical capillary length by 54 to 133 times. It is important to note that measuring the actual acting length is done manually, which results in a largely uncertain value due to the fluid flow which influences the particle motion in random directions and due to the difficulty of determining the exact moment where the two particles enter each other domain and start to attract. When the particles approach each other, in most cases, one or both would rotate around a vertical axis to the liquid surface to adjust their orientations before colliding. This phenomenon suggests that the contact line around the particles is non-uniform which further confirms the assumption of multipole model. Finally, the acting length was found to increase linearly with the critical radius of the two inclusion particles.

To calculate the capillary attraction force, an equilibrium was assumed between the capillary attraction force and the drag force due to the viscosity resistance of flow. The inertial force was first calculated, but it was negligibly small compared to the drag force (6 to 7 orders of magnitude less than the drag force). Thus, the inertial force was neglected in the calculations. Several capillary multipole orders were used in the calculations, and the most fitting model with the drag force was considered the best model to interpret the attraction force between the approaching inclusion particles. In most of the investigated inclusion clustering cases, the DP-QP model was the most fitting one when compared to the drag force.

5.1. Future work

The pictures obtained from the chemical extraction experiment showed that the alumina particles had quite irregular shapes, and some of them had faceted structures, which suggests that the currently used capillary interaction model is not ideally suitable to describe the behavior of alumina inclusions since it assumes a perfectly spherical shape of the inclusions. The DP model performs best among the investigated cases in this thesis. This model should be prohibited since it creates a dipole moment that will force the particle to spontaneously rotate to annihilate it. Therefore, for this model to apply on the inclusion particles their shapes should be more like disks instead of spheres. Accordingly, to achieve more accurate results, a modification to the Danov et al. model

is required. Another approach is to break down the inclusion particle into smaller spheres so that these small spheres will collectively have the shape of the inclusion particle [93].

Bibliography

[1] R. Kiessling, "Clean steel - a debatable concept," Metal Science, vol. 14, no. 4, pp. 161–172, 1980.

[2] A. L. V. d. Costa e Silva, "Non-metallic inclusions in steels – origin and control," *Journal of Materials Research and Technology*, vol. 7, no. 3, pp. 283–299, 2018.

[3] L. Zhang and B. G. Thomas, "State of the Art in Evaluation and Control of Steel Cleanliness," *ISIJ International*, vol. 43, no. 3, pp. 271–291, 2003.

[4] L. Zhang and S. Taniguchi, "Fundamentals of inclusion removal from liquid steel by bubble flotation," *International Materials Reviews*, vol. 45, no. 2, pp. 59–82, 2000.

[5] Y. Tanaka, F. Pahlevani, and V. Sahajwalla, "Agglomeration Behavior of Non-Metallic Particles on the Surface of Ca-Treated High-Carbon Liquid Steel: An In Situ Investigation," *Metals*, vol. 8, no. 3, p. 176, 2018.

[6] M. M. Nicolson, "The interaction between floating particles," *Mathematical Proceedings of the Cambridge Philosophical Society*, vol. 45, no. 2, pp. 288–295, 1949.

[7] V. N. Paunov, P. A. Kralchevsky, N. D. Denkov et al., "Lateral Capillary Forces between Floating Submillimeter Particles," *Journal of Colloid and Interface Science*, vol. 157, no. 1, pp. 100–112, 1993.

[8] H. Yin, H. Shibata, T. Emi et al., ""In-situ" Observation of Collision, Agglomeration and Cluster Formation of Alumina Inclusion Particles on Steel Melts," *ISIJ International*, vol. 37, no. 10, pp. 936–945, 1997.

[9] W. Mu, N. Dogan, and K. S. Coley, "Agglomeration of Non-metallic Inclusions at Steel/Ar Interface: In-Situ Observation Experiments and Model Validation," *Metallurgical and Materials Transactions B*, vol. 48, no. 5, pp. 2379–2388, 2017.

[10] Stamou, Duschl, and Johannsmann, "Long-range attraction between colloidal spheres at the air-water interface: the consequence of an irregular meniscus," *Physical review. E, Statistical physics, plasmas, fluids, and related interdisciplinary topics*, vol. 62, 4 Pt B, pp. 5263–5272, 2000.

[11] K. D. Danov, P. A. Kralchevsky, B. N. Naydenov et al., "Interactions between particles with an undulated contact line at a fluid interface: capillary multipoles of arbitrary order," *Journal of Colloid and Interface Science*, vol. 287, no. 1, pp. 121–134, 2005.

[12] B. Deo and R. Boom, *Fundamentals of steelmaking metallurgy*, 1993.

[13] A. L. V. d. Costa e Silva, "The effects of non-metallic inclusions on properties relevant to the performance of steel in structural and mechanical applications," *Journal of Materials Research and Technology*, vol. 8, no. 2, pp. 2408–2422, 2019.

[14] H. Yaguchi, "Effect of MnS inclusion size on machinabilty of low-carbon, leaded, resulfurized free-machining steel," *Journal of Applied Metalworking*, vol. 4, no. 3, pp. 214–225, 1986.

[15] Y. Chen, Y. Bao, M. Wang et al., "Superior machinability of steel enhanced with BN and MnS particles," *International Journal of Minerals, Metallurgy, and Materials*, vol. 23, no. 3, pp. 276–282, 2016.

[16] P. Vayrynen, S. Wang, S. Louthenkilpi et al., "Modeling and removal of inclusions in continuous casting," Materials and science technology, https://www.flow3d.com/wp-content/uploads/2014/08/Modeling-and-Removal-of-Inclusions-in-Continuous-Casting.pdf.

[17] S. Seetharaman, A. McLean, R. I. L. Guthrie et al., *Treatise on process metallurgy*, Elsevier, Amsterdam, 2014.

[18] Satyendra, "Effect of inlcusions on the properties of steel," Ispat guru, https://www.ispatguru.com/effect-of-inclusions-on-the-properties-of-steel/.

[19] K. C. L Zhang, "Project report: Cleanliness investigation of low carbon Al-killed steel in Bao Steel," BaoSteel, 1997, https://scholar.google.com/citations?user=rol80n4aaaaj&hl=en&oi=sra.

[20] Lifeng ZHANG, Brian G. THOMAS, Xinhua WANG, Kaike CAI, ed., *Evaluation and control of steel cleanliness-Review*, 2002.

[21] Asumadu Tabiri Kwayie, *Macro inclusion research: Detection and evaluation of macro inclusions in special steels,* Master's, Royal institute of Technology, 2012.

[22] E. Ruiz, D. Ferreño, M. Cuartas et al., "Machine Learning Methods for the Prediction of the Inclusion Content of Clean Steel Fabricated by Electric Arc Furnace and Rolling," *Metals*, vol. 11, no. 6, p. 914, 2021.

[23] L. Zhang, Q. Ren, H. Duan et al., "Modelling of non-metallic inclusions in steel," *Mineral Processing and Extractive Metallurgy*, vol. 129, no. 2, pp. 184–206, 2020.

[24] S. X. Li, "Effects of inclusions on very high cycle fatigue properties of high strength steels," *International Materials Reviews*, vol. 57, no. 2, pp. 92–114, 2012.

[25] P. Valentin, A. Bläsiusand C. Bruch, ed., *Conference on Cars and Trucks*, 2005.

[26] A. Srivastava, L. Ponson, S. Osovski et al., "Effect of inclusion density on ductile fracture toughness and roughness," *Journal of the Mechanics and Physics of Solids*, vol. 63, pp. 62–79, 2014.

[27] D. S. Sarma, A. V. Karasev, J&ouml et al., "On the Role of Non-metallic Inclusions in the Nucleation of Acicular Ferrite in Steels," *ISIJ International*, vol. 49, no. 7, pp. 1063–1074, 2009.

[28] T. E. Quested, "Understanding mechanisms of grain refinement of aluminium alloys by inoculation," *Materials Science and Technology*, vol. 20, no. 11, pp. 1357–1369, 2004.

[29] N. Ånmark, A. Karasev, and P. G. Jönsson, "The Effect of Different Non-Metallic Inclusions on the Machinability of Steels," *Materials (Basel, Switzerland)*, vol. 8, no. 2, pp. 751–783, 2015.

[30] *IISI Study on Clean Steel: State of the Art and Process Technology in Clean Steelmaking*, 2004.

[31] R. Emadi and A. Monshi, "Cold Isostatic Pressing of Alumina-Graphite Castables, a New Technology to Manufacture Special Refractories," *ISIJ International*, vol. 44, no. 10, pp. 1679–1685, 2004.

[32] A. F. Dick, X. Yu, R. J. Pomfret et al., "Attack of Submerged Entry Nozzles by Mould Flux and Dissolution of Refractory Oxides in the Flux," *ISIJ International*, vol. 37, no. 2, pp. 102–108, 1997.

[33] C. Pfeiler, M. Wu, and A. Ludwig, "Influence of argon gas bubbles and non-metallic inclusions on the flow behavior in steel continuous casting," *Materials Science and Engineering: A*, 413-414, pp. 115–120, 2005.

[34] L. Zhang, Y. Wang, and X. Zuo, "Flow Transport and Inclusion Motion in Steel Continuous-Casting Mold under Submerged Entry Nozzle Clogging Condition," *Metallurgical and Materials Transactions B*, vol. 39, no. 4, pp. 534–550, 2008.

[35] F. Marquis, *Proceedings of the 8th Pacific Rim International Congress on Advanced Materials and Processing*, Springer International Publishing, Cham, 2016.

[36] Uxía Diéguez Salgado, *Investigation of particle attraction by steel/refractory Investigation of particle attraction by steel/refractory and steel/gas interfaces and the associated relevance for clogging in casting processes for clogging in casting processes,* Degree of doctor of Philosophy in Mining and Metallurgical Sciences, Montanuniversität, 2018.

[37] X. Yang, J. Yu, Z. Liu et al., "The charged characteristics of the submerged entry nozzle used for continuous casting," *Ceramics International*, vol. 43, no. 2, pp. 2881–2883, 2017.

[38] K. G. Rackers and B. G. Thomas, ed., *Clogging in continuous casting nozzles*, 1995.

[39] S. R. Cameron, ed., *The reduction of Tundish nozzle clogging during continuous casting at Dofasco*, 1992, April.

[40] F. Hauck and J. Pötschke, "Der Verschleiß von Tauchausgüssen beim Stranggießen von Stahl," *Archiv für das Eisenhüttenwesen*, vol. 53, no. 4, pp. 133–138, 1982.

[41] J. Poirier, M. A. Guiban, P. Tassot, E. Hanse, B. Thillo and, P., ed., Tokyo, 1995.

[42] Y. Vermeulen, B. Coletti, B. Blanpain et al., "Material Evaluation to Prevent Nozzle Clogging during Continuous Casting of Al Killed Steels," *ISIJ International*, vol. 42, no. 11, pp. 1234–1240, 2002.

[43] J. Ikäheimonen, K. Leiviskä, J. Ruuska et al., "NOZZLE CLOGGING PREDICTION IN CONTINUOUS CASTING OF STEEL," *IFAC Proceedings Volumes*, vol. 35, no. 1, pp. 143–147, 2002.

[44] Hans F Schrewe, *Continuous casting of steel: fundamental principles and practice*, 1989.

[45] Faulring, Gloria M., and FARRELL JW, "Steel flow through nozzles: influence of calcium," 1980.

[46] J Knoepke, M Hubbard, J Kelly, R Kittridge, J Lucas, ed., *Pencil blister reduction at inland steel company*, 1994.

[47] M. Lind and L. Holappa, "Transformation of Alumina Inclusions by Calcium Treatment," *Metallurgical and Materials Transactions B*, vol. 41, no. 2, pp. 359–366, 2010.

[48] D.-Z. Lu, G.A. Irons, and W.-K. Lu, "Kinetics, mechanisms and modelling of calcium treatment of steel," *Scaninject*, VI, 293-63, 1992.

[49] K. N. PA Kralchevskya, "Capillary interactions between particles Capillary interactions between particles bound to interfaces, liquid films and biomembranes," 2000.

[50] G. Wang, A. V. Nguyen, S. Mitra et al., "A review of the mechanisms and models of bubble-particle detachment in froth flotation," *Separation and Purification Technology*, vol. 170, pp. 155–172, 2016.

[51] E. A. Boucher, M. J. Evans, and T. G. J. Jones, "Adv. Colloid Interface Sci.," 27 (1-2), 43-79., 1987.

[52] James G. Speight, ed., *Natural Water Remediation*: *2- The properties of water*, Elsevier, 2020.

[53] Georgia state university, "Surface tension," http://hyperphysics.phy-astr.gsu.edu/hbase/surten.html.

[54] M. V. Berry, "The molecular mechanism of surface tension," *Physics Education*, vol. 6, no. 2, pp. 79–84, 1971.

[55] D. Vella and L. Mahadevan, "The "Cheerios effect"," *American Journal of Physics*, vol. 73, no. 9, pp. 817–825, 2005.

[56] P. A. Kralchevsky and K. Nagayama, "Capillary interactions between particles bound to interfaces, liquid films and biomembranes," *Advances in Colloid and Interface Science*, vol. 85, 2-3, pp. 145–192, 2000.

[57] P. Kralchevsky, V. Paunov, I. Ivanov et al., "Capillary meniscus interaction between colloidal particles attached to a liquid—fluid interface," *Journal of Colloid and Interface Science*, vol. 151, no. 1, pp. 79–94, 1992.

[58] X. Zhou and F. Zhang, "Bifurcation of a partially immersed plate between two parallel plates," *Journal of Fluid Mechanics*, vol. 817, pp. 122–137, 2017.

[59] R. Förch, H. Schönherr, and A. T. A. Jenkins, *Surface design*: *Applications in bioscience and nanotechnology / edited by Renate Forch, Holger Schonherr, A. Tobias A. Jenkins*, Wiley-VCH, Weinheim, 2009.

[60] A. Maestro, E. Guzmán, F. Ortega et al., "Contact angle of micro- and nanoparticles at fluid interfaces," *Current Opinion in Colloid & Interface Science*, vol. 19, no. 4, pp. 355–367, 2014.

[61] Z. Shi, Y. Zhang, M. Liu et al., "Dynamic contact angle hysteresis in liquid bridges," *Colloids and Surfaces A: Physicochemical and Engineering Aspects*, vol. 555, pp. 365–371, 2018.

[62] H. B. Eral, D. J. C. M. 't Mannetje, and J. M. Oh, "Contact angle hysteresis: a review of fundamentals and applications," *Colloid and Polymer Science*, vol. 291, no. 2, pp. 247–260, 2013.

[63] C. Camoin, J. F. Roussell, R. Faure et al., "Mesure des Forces D'Attraction Entre Sphères Partiellement Immergées: Influence des Interfaces," *Europhysics Letters (EPL)*, vol. 3, no. 4, pp. 449–457, 1987.

[64] O. D. Velev, N. D. Denkov, V. N. Paunov et al., "Direct measurement of lateral capillary forces," *Langmuir : the ACS journal of surfaces and colloids*, vol. 9, no. 12, pp. 3702–3709, 1993.

[65] Dushkin, Kralchevsky, Yoshimura et al., "Lateral capillary forces measured by torsion microbalance," *Physical review letters*, vol. 75, no. 19, pp. 3454–3457, 1995.

[66] J. T. Petkov, N. D. Denkov, K. D. Danov et al., "Measurement of the Drag Coefficient of Spherical Particles Attached to Fluid Interfaces," *Journal of Colloid and Interface Science*, vol. 172, no. 1, pp. 147–154, 1995.

[67] J. Lucassen, "Capillary forces between solid particles in fluid interfaces," *Colloids and Surfaces*, vol. 65, 2-3, pp. 131–137, 1992.

[68] M. G. Nikolaides, A. R. Bausch, M. F. Hsu et al., "Electric-field-induced capillary attraction between like-charged particles at liquid interfaces," *Nature*, vol. 420, no. 6913, pp. 299–301, 2002.

[69] E. L. Decker and S. Garoff, "Contact Line Structure and Dynamics on Surfaces with Contact Angle Hysteresis," *Langmuir : the ACS journal of surfaces and colloids*, vol. 13, no. 23, pp. 6321–6332, 1997.

[70] J. C. Loudet, A. G. Yodh, and B. Pouligny, "Wetting and contact lines of micrometer-sized ellipsoids," *Physical review letters*, vol. 97, no. 1, p. 18304, 2006.

[71] Brown, Smith, and Rennie, "Fabricating colloidal particles with photolithography and their interactions at an air-water interface," *Physical review. E, Statistical physics, plasmas, fluids, and related interdisciplinary topics*, vol. 62, 1 Pt B, pp. 951–960, 2000.

[72] "Drag Force Formula," Topper, https://www.toppr.com/guides/physics-formulas/drag-force-formula/.

[73] G. Falkovich, *Fluid mechanics*, Cambridge University Press, Cambridge, 2018.

[74] K. Danov, R. Aust, F. Durst et al., "Influence of the Surface Viscosity on the Hydrodynamic Resistance and Surface Diffusivity of a Large Brownian Particle," *Journal of Colloid and Interface Science*, vol. 175, no. 1, pp. 36–45, 1995.

[75] A. Dani, G. Keiser, M. Yeganeh et al., "Hydrodynamics of Particles at an Oil-Water Interface," *Langmuir : the ACS journal of surfaces and colloids*, vol. 31, no. 49, pp. 13290–13302, 2015.

[76] M.-A. van Ende, *Formation and morphology of non-metallic inclusions in aluminium killed steels*, UCL - Université Catholique de Louvain.

[77] D. Janis, R. Inoue, A. Karasev et al., "Application of Different Extraction Methods for Investigation of Nonmetallic Inclusions and Clusters in Steels and Alloys," *Advances in Materials Science and Engineering*, vol. 2014, pp. 1–7, 2014.

[78] R. G. Smerko and D. A. Flinchbaugh, "Recent Progress in the Chemical Extraction of Nonmetallic Inclusions in Steel—Techniques and Applications," *JOM*, vol. 20, no. 7, pp. 43–51, 1968.

[79] R. Dekkers, B. Blanpain, P. Wollants et al., "Non-metallic inclusions in aluminium killed steels," *Ironmaking & Steelmaking*, vol. 29, no. 6, pp. 437–444, 2002.

[80] Erik Luyk, "Backscattered Electrons in SEM Imaging," Thermo Fisher scientific, https://www.thermofisher.com/blog/materials/backscattered-electrons-in-sem-imaging/.

[81] G. E. Lloyd, "Atomic number and crystallographic contrast images with the SEM: a review of backscattered electron techniques," *Mineralogical Magazine*, vol. 51, no. 359, pp. 3–19, 1987.

[82] P. D. Ngo, "Energy Dispersive Spectroscopy," in *Failure Analysis of Integrated Circuits,* L. C. Wagner, Ed., pp. 205–215, Springer US, Boston, MA, 1999.

[83] A. Canette and R. Briandet, "MICROSCOPY | Confocal Laser Scanning Microscopy," in *Encyclopedia of Food Microbiology*, pp. 676–683, Elsevier, 2014.

[84] B. V. R. Tata and B. Raj, "Confocal laser scanning microscopy: Applications in material science and technology," *Bulletin of Materials Science*, vol. 21, no. 4, pp. 263–278, 1998.

[85] P. T. Jones, D. Desmet, M. Guo et al., "Using confocal scanning laser microscopy for the in situ study of high-temperature behaviour of complex ceramic materials," *Journal of the European Ceramic Society*, vol. 27, no. 12, pp. 3497–3507, 2007.

[86] H. Yin, H. Shibata, T. Emi et al., "Characteristics of Agglomeration of Various Inclusion Particles on Molten Steel Surface," *ISIJ International*, vol. 37, no. 10, pp. 946–955, 1997.

[87] Marie-Aline Van ende, *Formation and Morphology of non-metallic inclusions in aluminum killed steel,* Phd, Faculty of Engineering Science, January/ 2010.

[88] W. Mu, N. Dogan, and K. S. Coley, "In situ observation of deformation behavior of chain aggregate inclusions: a case study for Al2O3 at a liquid steel/argon interface," *Journal of Materials Science*, vol. 53, no. 18, pp. 13203–13215, 2018.

[89] K. Nakajima and S. Mizoguchi, "Capillary interaction between inclusion particles on the 16Cr stainless steel melt surface," *Metallurgical and Materials Transactions B*, vol. 32, no. 4, pp. 629–641, 2001.

[90] I. Jimbo and A. W. Cramb, "The density of liquid iron-carbon alloys," *Metallurgical and Materials Transactions B*, vol. 24, no. 1, pp. 5–10, 1993.

[91] A. Kasama, A. McLean, W. A. Miller et al., "Surface Tension of Liquid Iron and Iron-Oxygen Alloys," *Canadian Metallurgical Quarterly*, vol. 22, no. 1, pp. 9–17, 1983.

[92] L. Zheng, A. Malfliet, P. Wollants et al., "Effect of Alumina Morphology on the Clustering of Alumina Inclusions in Molten Iron," *ISIJ International*, vol. 56, no. 6, pp. 926–935, 2016.

[93] Z. Qiu, A. Malfliet, B. Blanpain et al., "Capillary Interaction Between Arbitrarily-Shaped Inclusions at the Gas/Steel Interface," *Metallurgical and Materials Transactions B*, vol. 53, no. 3, pp. 1894–1903, 2022.